

RESEARCH ARTICLE OPEN ACCESS

Mapping the Spatial Scales of Australian Extreme Precipitation Using Daily Rain Gauges

Dongqi Lin^{1,2} | Kate R. Saunders^{1,3} | Martin S. Singh^{2,4}

¹ARC Centre of Excellence for Climate Extremes, Monash University, Melbourne, Victoria, Australia | ²School of Earth, Atmosphere and Environment, Monash University, Melbourne, Victoria, Australia | ³Department of Econometrics and Business Statistics, Monash University, Melbourne, Victoria, Australia | ⁴ARC Centre of Excellence for Weather of the 21st Century, Monash University, Melbourne, Victoria, Australia

Correspondence: Dongqi Lin (dongqi.lin@monash.edu)

Received: 5 September 2025 | **Revised:** 13 January 2026 | **Accepted:** 27 January 2026

Keywords: climate variability | climatology | extreme precipitation | spatial scales | spatial statistics

ABSTRACT

The impacts of extreme precipitation events (EPEs) on society are strongly influenced by their spatial footprint, yet the spatial scales of such events remain underexplored. Here we present the first continent-wide analysis of the spatial scales of daily EPEs in Australia. We estimate the characteristic spatial scale of EPEs seasonally across the Australian continent using daily station observations and semivariograms. A semivariogram is a spatial statistical function that measures how spatial autocorrelation in precipitation decays with distance. Consistent with global analyses of satellite data, EPEs generally have larger spatial scales at higher latitudes. However, our analysis reveals complex seasonal and geographical dependencies that highlight the role of topography and meteorological regimes. We also analyse EPE spatial scales under different phases of the El Niño–Southern Oscillation (ENSO). In SON and DJF, southeastern Australia exhibits larger spatial scales during La Niña, although no uniform pattern is observed across the continent. Long-term changes were analysed using 2070 stations with continuous operation between 1960 and 2023. Southwestern Australia shows a notable reduction in median EPE length scale in most seasons, while eastern regions exhibit a decrease in MAM and an increase in SON. Together, these findings provide a new climatological reference for the spatial scale of EPEs in Australia. These results also highlight the need to better understand the physical factors controlling the spatial scale of precipitation extremes in current and future climates.

1 | Introduction

The impacts of extreme precipitation events (EPEs) are strongly modulated by their spatial footprint (e.g., Schaller et al. 2016; Touma et al. 2018; Bevacqua et al. 2021, and citations therein). For example, widespread EPEs can lead to spatially extensive floods affecting multiple regions simultaneously, amplifying societal impacts across broader geographic areas (Jongman et al. 2014; Berghuijs et al. 2019). In contrast, localised extremes may cause intense but spatially confined impacts, such as flash flooding, which often overwhelm local infrastructure and are harder to predict due to short lead times and high spatial variability (e.g., Schumacher 2017). Although many studies have

focused on the frequency and intensity of EPEs, relatively few have explored their spatial extent (Hoegh-Guldberg et al. 2018; Bevacqua et al. 2021).

The characteristics of EPEs are expected to change in a warming climate (O’Gorman 2015). As the atmosphere warms, it becomes moister, favouring more intense precipitation, while shifts in large-scale circulation patterns may alter both precipitation intensity and spatial patterns (O’Gorman and Schneider 2009; Bevacqua et al. 2020). Several studies have examined how the spatial extent of EPEs responds to warming, but no clear consensus has emerged from modelling and observational approaches. In modelling studies,

This is an open access article under the terms of the [Creative Commons Attribution](https://creativecommons.org/licenses/by/4.0/) License, which permits use, distribution and reproduction in any medium, provided the original work is properly cited.

© 2026 The Author(s). *International Journal of Climatology* published by John Wiley & Sons Ltd on behalf of Royal Meteorological Society.

Chang et al. (2016) reported a reduction in storm size under a warmer climate, whereas Guinard et al. (2015) and Dwyer and O’Gorman (2017) found that the precipitation structures increase in size with warming. Observational analyses of the present-day climate have also yielded different findings for the relationship between rainfall spatial extent and atmospheric conditions: Wasko et al. (2016) observed a decrease in storm size with increasing local temperatures using hourly observations in Australia, while Lochbihler et al. (2017) identified a positive relationship between rain cell size and dew point temperature in the Netherlands. At a broader temporal and spatial scale, a global trend analysis by Tan et al. (2021) found that the spatial extent of daily EPEs increased from 1983 to 2018 in non-monsoon regions of the Northern Hemisphere.

Beyond the divergent findings across existing studies, the spatial scales of extreme precipitation remain underexplored. Australia is one of the many regions that still lack a baseline characterisation of the spatial extent of EPEs in the current climate. While Australian rainfall is “more variable than could be expected from similar climates elsewhere in the world” (Nicholls et al. 1997), many existing studies of precipitation extremes focus on specific subregions without explicitly addressing spatial scales (e.g., Warren et al. 2021; White et al. 2022). Some limited analysis has been done at the hourly level by Wasko et al. (2016). They estimated storm sizes using hourly station data from a small number of stations (93 for one-hour events and 78 for three-hour events) in Australia, thereby restricting their spatial representativeness. On the daily scale, Saunders et al. (2021) used annual maxima to identify regions that are likely to be similarly affected by EPEs for Australia. However, annual maxima at different locations do not necessarily occur on the same day, which limits their utility for analysing the spatial extent of extremes.

To address this existing gap, this study provides a climatological assessment of EPE spatial extent across the Australian continent using daily rain gauge data. A well-defined climatology enables an assessment of the mean structure and variability of EPEs. This provides a foundation for investigating the physical mechanisms that govern their spatial extent. Long-term gauge measurements also allow us to evaluate how EPE spatial scales respond to internal climate variability and provide estimates of long-term trends.

Although a global EPE spatial scale analysis was recently developed by Tan et al. (2021) using satellite observations, our analysis relies on in situ rain gauge data. While gauge-based estimates are subject to measurement errors and are constrained by limited spatial coverage, they ensure greater accuracy in capturing precipitation extremes and provide the advantage of long observational records. Satellite-based products often exhibit precipitation estimation errors when compared to ground measurements (Alexander et al. 2020). For example, Tansey et al. (2022) found that satellite products tend to overestimate seasonal total liquid precipitation; Montoya Duque et al. (2023) reported an overestimation of precipitation intensity in the Southern Ocean; and Ponukumati et al. (2023) showed that satellite-based products can overestimate extreme rainfall intensity relative to daily automatic weather station measurements in India. These errors limit the reliability of satellite products for analysing precipitation extremes. Compared to rain gauges, satellite products are

also suboptimal for long-term analyses of extreme events. Most satellite-based precipitation missions were launched after the 1980s (e.g., Simpson et al. 1996; Ashouri et al. 2015), and typically provide only one or two observations per day, while many rain gauges in Australia were deployed in the early 1900s (see Figure S1).

Gridded rainfall products, typically constructed by interpolating in situ gauge observations to a regular grid, are also widely used to analyse precipitation extremes. For instance, the Australian Gridded Climate Data (AGCD; Evans et al. 2020; Jones et al. 2009) is the Bureau of Meteorology’s (BoM) official land-based rainfall dataset, and has been applied in many extreme rainfall studies (e.g., Domeisen et al. 2022; Irving et al. 2024). Similar gridded products have been applied in EPE analyses in other countries, including Italy (Grazzini et al. 2020) and India (Nikumbh et al. 2019). However, gridded products do not usually perform well over areas with low station density and can underestimate the intensity and frequency of local extremes (King et al. 2013). Therefore, using rain gauge data allows for a more direct and physically consistent identification of EPEs.

To estimate spatial scales, we adopt the semivariogram approach introduced by Touma et al. (2018). Originating in spatial statistics, a semivariogram describes how the spatial dependence in a variable, such as precipitation, weakens as the distance between two locations increases. It provides an estimate of the distance over which the variable remains correlated (Cressie 2015). This estimate serves as a quantitative indicator of the spatial scales of EPEs. This semivariogram approach was first used to characterise the spatial scales of EPEs across the United States using the Global Historical Climatology Network-Daily (GHCN-D) station dataset (Touma et al. 2018). It was further extended by Touma et al. (2019) to assess the spatial extent of tropical cyclones, and more recently adopted for the global satellite-based EPE spatial scale study by Tan et al. (2021).

Building on the existing semivariogram-based work, we use all stations available from the BoM’s daily rain gauges (9861 in total) to derive a long-term climatology of the EPE spatial scales for the Australian continent. Since ENSO is the main driver of interannual rainfall variability in northern and eastern Australia (e.g., McBride and Nicholls 1983; Risbey et al. 2009; King et al. 2020; Gillett et al. 2023; Tozer et al. 2023; McGregor et al. 2024; Huang et al. 2024; He et al. 2025), we further examine how the EPE spatial scale differs between El Niño and La Niña periods. Finally, we leverage the long-term record of daily rain gauge observations to assess changes in EPE spatial scales over time. Our findings show that the seasonal patterns, ENSO relationships, and long-term trends in EPE spatial scales vary across the continent but differ from those of mean precipitation and those of the intensity of precipitation extremes. In particular, increases in spatial scale do not consistently occur during “wetter” periods or in “wetter” regions. This suggests that different physical processes govern the intensity and spatial extent of precipitation extremes, and that these characteristics may respond differently to climate change.

The remainder of this paper is structured as follows. Section 2 describes the rain gauge dataset, the semivariogram approach used to estimate the EPE spatial scales, ENSO classification,

and trend analysis methodology. Section 3 presents our results on the spatial scales of EPEs, including their regional and seasonal variability, relationship with ENSO, and long-term trends. Sections 4 and 5 provide discussions and conclusions, respectively.

2 | Data and Methods

2.1 | Data for Analysing Seasonal EPEs

We used daily rain gauge observations obtained from the weather station directory operated by the BoM for the period between 1940 and 2024. The BoM daily rainfall observations are made at 0900 local time, recording the preceding 24-h total precipitation. The earliest rain gauge record in the BoM archive started in May 1826. The number of active BoM stations in Australia over time is shown in Figure S1.

To estimate the climatological length scales of EPEs, we need stations that have continuous data availability, a sufficiently long period of record, and satisfactory data quality and station density. To balance these factors, we chose the period from 1940 to 2024 for analysis. Only stations with an operation period of more than 20 years were included. A total of 9861 stations met this criterion between 1940 and 2024. The locations of these stations are shown in Figure 1a.

The stations are grouped using the 15 natural resource management (NRM) sub-clusters, which are administrative regions used for the Australian Government's environment and sustainable agriculture programs (CSIRO 2015). These regions provide a standardised geographic framework widely used in environmental assessments across Australia. Considering the climate characteristics and spatial station distribution in the rangelands (central Australia), we divide the rangeland region into western (RW) and eastern (RE) clusters along the 130°E longitude,

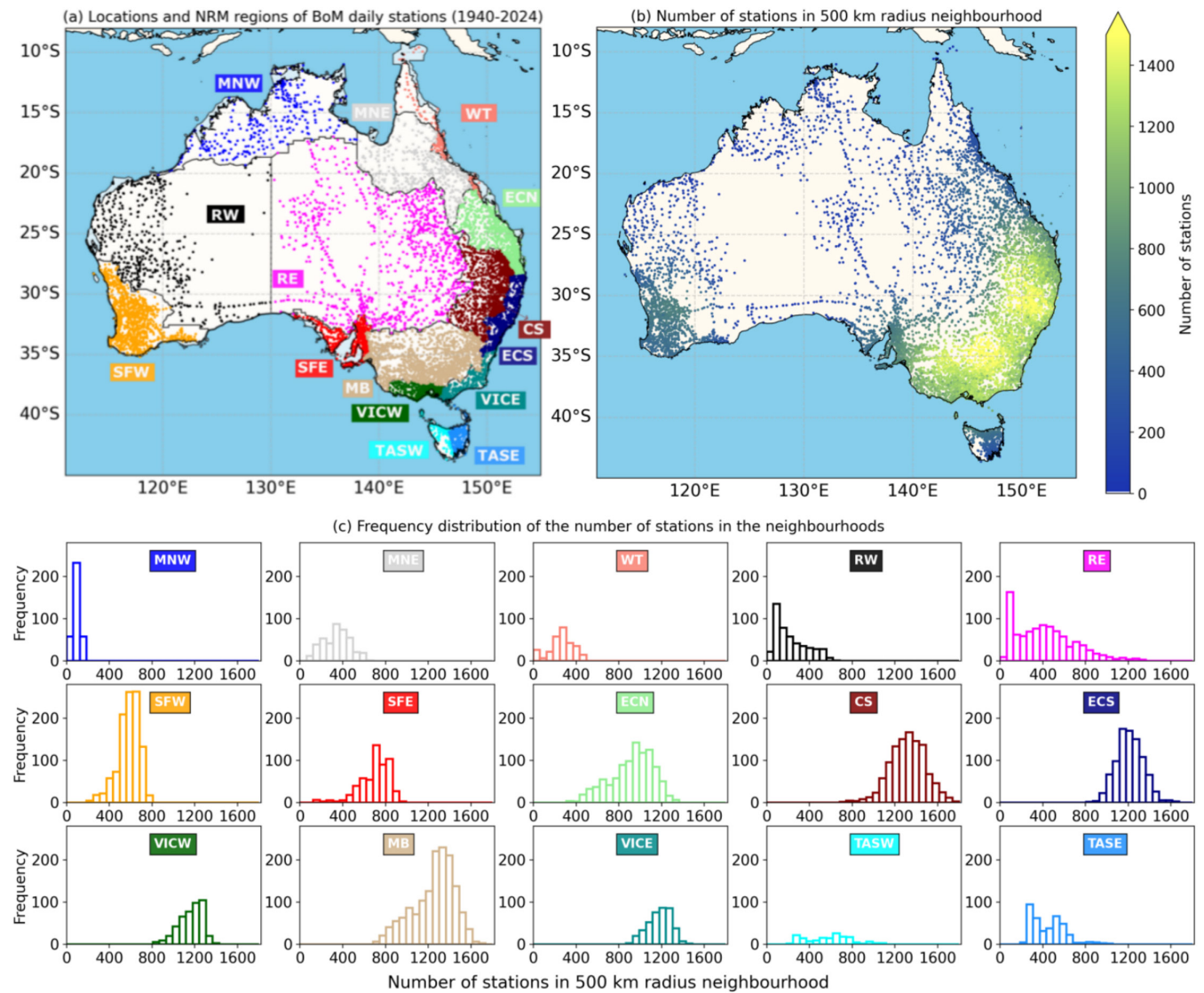


FIGURE 1 | (a) Locations of BoM daily stations with more than 20 years of continuous records between 1940 and 2024 coloured by their NRM regions. (b) The average number of stations used in each 500-km radius neighbourhood for P90 semivariogram analysis. (c) Frequency distribution of the number of stations in the 500-km radius neighbourhoods in each NRM region, as shown in Panel (a).

TABLE 1 | Acronyms for the NRM sub-clusters shown in Figure 1. Note that the Rangeland has been split into Rangeland West and Rangeland East due to the natural separation of station locations.

Acronym	NRM sub-clusters
MNW	Monsoonal North West
MNE	Monsoonal North East
WT	Wet Tropics
RW	Rangeland West
RE	Rangeland East
SFW	Southern Flatlands West
SFE	Southern Flatlands East
ECN	East Coast North
CS	Central Slopes
ECS	East Coast South
VICW	Victoria West
MB	Murray Basin
VICE	Victoria East
TASW	Tasmania West
TASE	Tasmania East

replacing the original north and south rangeland clusters from the NRM classification (see CSIRO 2015). The acronyms for the NRM sub-clusters are given in Table 1.

To identify daily extremes, we define each station's seasonal 90th percentile of rainy days (precipitation > 1 mm day⁻¹) as its extreme precipitation threshold (hereafter “P90”). Conditioning on rainy days avoids including weak rainfall in dry regions and prevents clustering events in a single season. This also helps avoid data quality issues associated with small rainfall amounts including condensation/dew or other non-rain events being recorded as rainfall, and mechanical issues that affect gauge operation (e.g., Dunn et al. 2025). An EPE is recorded when daily precipitation meets or exceeds the station's seasonal P90. We have conducted sensitivity tests using monthly, seasonal, and full-record P90 thresholds (not shown). Regardless of the threshold chosen, the overall spatial and regional patterns remain consistent, confirming that our conclusions are robust to the choice of threshold. Here, we used the seasonal P90 instead of the monthly P90 as in Touma et al. (2018) and Tan et al. (2021) because this better reflects seasonal climatology and avoids including moderately heavy events from drier months in the analysis.

The P90 values across each season and each station are shown in Figure 2. Hereafter, to avoid overplotting in regions with high station density, station data are averaged into 40-km

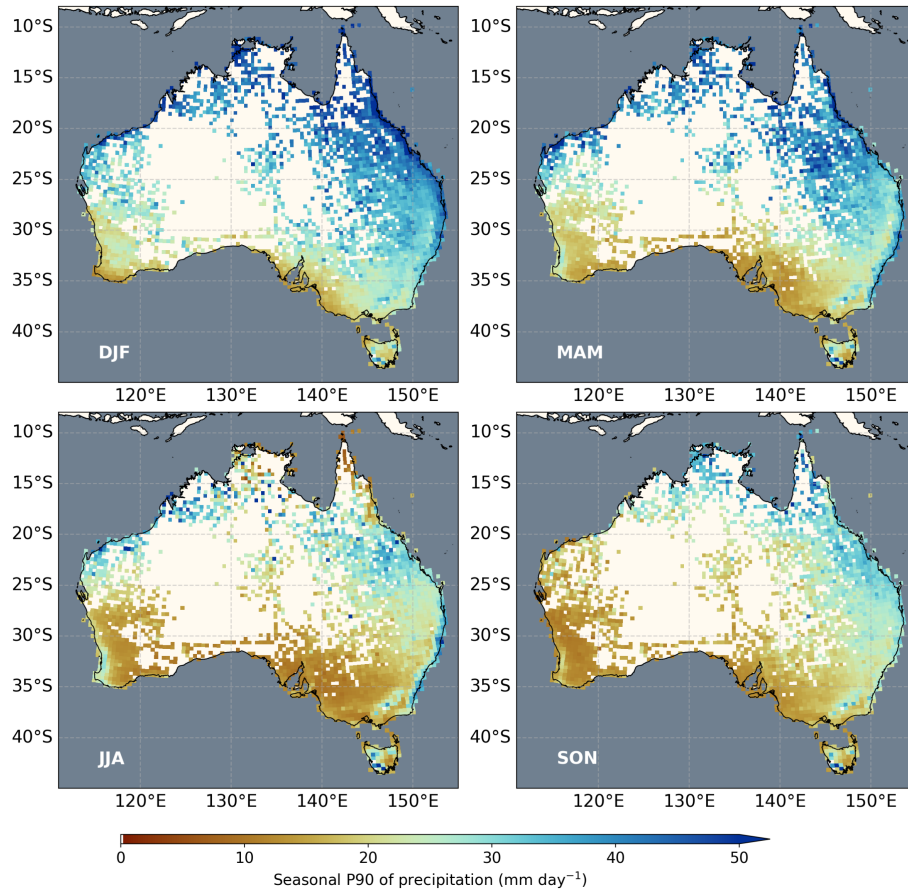


FIGURE 2 | Seasonal 90th percentile (P90) of daily precipitation accumulation for DJF (top left), MAM (top right), JJA (bottom left), and SON (bottom right).

grid boxes. The box size was chosen to provide a balanced representation of both dense and sparse regions. These gridded data are used only for visualisation purposes, while all analyses were performed using the original station-level data. The seasonal variation in P90 magnitudes reflects well-known rainfall patterns across Australia, with the highest values occurring in DJF and much lower values in JJA (e.g., Drosowsky 1993), even for parts of southern Australia where mean rainfall is higher in JJA than in DJF (Figure S2). This seasonality is particularly pronounced in Northern Australia, where the monsoon brings most rainfall between October and April. During the monsoon inactive phase (May–September), most JJA days in Northern Australia are dry, and rainfall amounts on wet days are low, resulting in a lower P90 magnitude. The P90 threshold map for JJA (Figure 2) appears less spatially coherent across northern Australia due to the limited sample size during the dry season (see Figure 6 and discussion in Section 3.1). In southern Australia, the relatively low P90 thresholds in JJA result from the use of seasonal P90 values, which naturally reflect the modest winter rainfall amounts in this region. These seasonal variations in the P90 thresholds are not evident in the global study by Tan et al. (2021), possibly because their satellite study examined spatially averaged precipitation over $0.25^\circ \times 0.25^\circ$ regions rather than gauge measurements.

2.2 | Estimating the Spatial Scales of EPEs

2.2.1 | Data Preparation for Spatial Scale Estimation

To estimate the spatial scale of EPEs, the daily precipitation data were first converted into a binary EPE dataset. At each station, observations were assigned a value of 1 if their daily precipitation is greater than or equal to the seasonal P90 threshold, and 0 otherwise. We did not retain precipitation amounts because the magnitude of extremes is relative to geographical context and can vary with measurement instrumentation, especially across a continent as large as Australia. By using binary data, the impacts of EPEs can be compared across regions, whereas raw precipitation amounts vary greatly across Australia (see Figure 2).

To identify stations impacted by the same EPE, we define a 500-km radius neighbourhood around each station (see black and red dots in Figure 3a,c). On days when the neighbourhood central station exceeds its seasonal P90 threshold, all stations within this neighbourhood are paired and classified into the following categories:

1. 1–1 pair: two stations both detected an EPE on the same day.
2. 1–0 pair: only one of the two stations detected an EPE on that particular day.
3. 0–0 pair: the EPE was observed at neither station on that day.

The 0–0 pairs are discarded as they are not needed in the subsequent analysis, similar to Touma et al. (2018). Figure 3a,c demonstrates these pair categories: any two red stations are

classified as a 1–1 pair; a red and a black station as a 1–0 pair; and two black stations as a 0–0 pair.

This approach of pair selection does not account for EPEs that occur beyond the neighbourhood boundary. To address this, we allowed for relaxed neighbourhood pairing, meaning that one of the stations in a pair could lie outside the 500-km neighbourhood. This is illustrated in Figure 3a,c (pink and grey dots). Only pairs where at least one station lies within the 500-km neighbourhood (i.e., red–pink, red–grey, and black–pink pairs) were retained. Pairs entirely outside the 500-km radius were excluded.

The choice of neighbourhood size is a key consideration, as previous studies have shown it can influence the absolute magnitude of estimated spatial scales, although the relative regional and seasonal variations remain largely unchanged (Touma et al. 2018). On this basis, we conservatively adopt a 500-km radius, consistent with physical reasoning that this scale is sufficient to capture the spatial extent of many mesoscale systems (e.g., Khouakhi et al. 2017; Tan et al. 2021). The number of stations used for EPE spatial scale analysis within the 500-km neighbourhoods for each station and NRM region is summarised in Figure 1b,c.

2.2.2 | Semivariogram Estimation Using the Binary EPE Dataset

To quantify the EPE spatial scales, a semivariogram is used to characterise the degree of spatial autocorrelation of a given spatial field $Z(x)$ at location x by describing how the similarity between observations decreases as the distance h between them increases. It is defined as the expected squared difference between values separated by distance h :

$$\gamma(h) = \frac{1}{2} \mathbb{E} [Z(x) - Z(x+h)]^2 \quad (1)$$

where h is the distance between the two locations (Webster and Oliver 2007). This form of the semivariogram assumes isotropy, which means that the spatial relationships depend only on the distance between locations, not on their spatial orientation relative to one another.

As the EPE dataset is now binary, $Z(x)$ only takes values of 0 or 1. This means the pointwise estimate of $\gamma(h)$ for any two stations x_i and x_j is 0 for a 1–1 pair, and 0.5 for a 1–0 pair. To empirically estimate $\gamma(h)$, we require an approach suited to binary data, irregularly spaced stations, and changing network coverage.

To address this, the observations can be pooled to estimate the semivariogram empirically. We group station pairs (1–1 and 1–0) based on their distance apart, using 25-km bins within a 500-km neighbourhood, following Touma et al. (2018) and Tan et al. (2021). The grouping intervals are therefore (0, 25] km, (25, 50] km, ... (475, 500] km. For any interval $(h - \delta, h]$, where $\delta = 25$ km is the bin size, this can be written as:

$$\mathcal{N}_h = \{ (x_i, x_j) : h - \delta < d(x_i, x_j) \leq h; i, j = 1, \dots, S \} \quad (2)$$

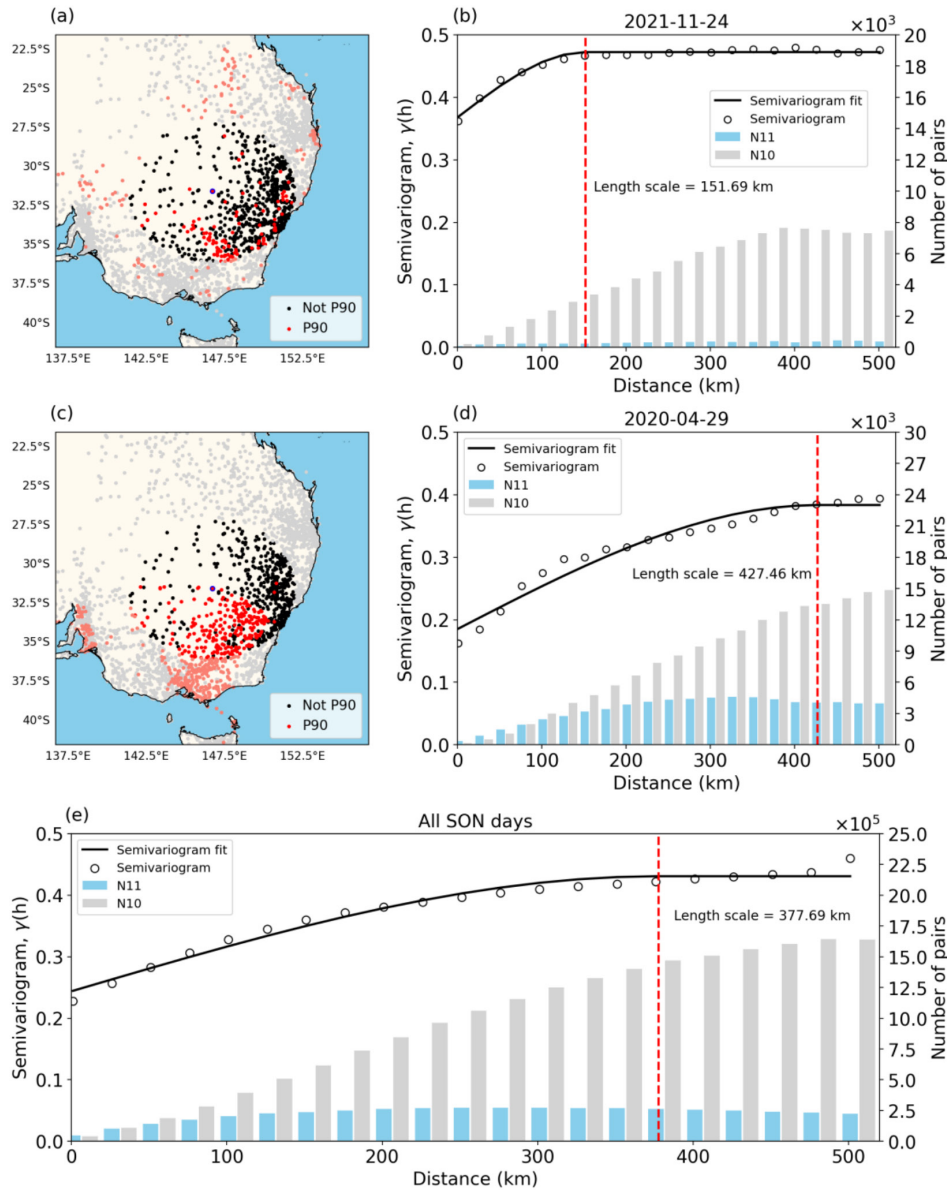


FIGURE 3 | Illustration of the relaxed moving neighbourhood method for a station in New South Wales, Australia. Two examples are given for the EPE on 24th November 2021 (a, b), and a larger EPE on 29th April 2020 (c, d). Panels (a) and (c) are maps illustrating stations within the 500-km radius neighbourhood in red (P90 detected) and black (P90 not detected). Stations outside the neighbourhood are shown in pink (P90 detected and outside) and grey (P90 not detected and outside). Panels (b) and (d) show the semivariogram estimation for the 2 days. The blue bars represent the number of 1–1 pairs, and the grey bars are for 1–0 pairs. The red dashed line shows the derived length scale. Panel (e) illustrates the climatological length scale for the station in SON. The blue and grey bars are the sum of all 1–1 pairs and 1–0 pairs over the 67 extreme days in SON for that station, respectively.

where S is the total number of stations in the relaxed neighbourhood, $d(x_i, x_j)$ is the Euclidean distance between stations x_i and x_j . This produces a series of sets containing grouped station pairs $\mathcal{N}_{25}, \mathcal{N}_{50}, \dots, \mathcal{N}_{500}$.

By changing the expectation in Equation (1) to a sum, the empirical estimate of the semivariogram for a given binned interval is

$$\hat{\gamma}\left(h - \frac{\delta}{2}\right) = \frac{1}{2|\mathcal{N}_h|} \sum_{(x_i, x_j) \in \mathcal{N}_h} [Z(x_i) - Z(x_j)]^2 \quad (3)$$

where $h - \frac{\delta}{2}$ is used because estimates are taken at the bin centre. The notation $|\mathcal{N}_h|$ means the total number of distinct station pairs in the set \mathcal{N}_h . As the pairs fall into one of two distinct categories (1–0 and 1–1 pairs), this can also be written as $|\mathcal{N}_h| = |\mathcal{N}_{h,(1,0)}| + |\mathcal{N}_{h,(1,1)}|$.

As $Z(x)$ is a binary field, the above equation further simplifies to

$$\hat{\gamma}\left(h - \frac{\delta}{2}\right) = \frac{1}{2} \left(\frac{|\mathcal{N}_{h,(1,0)}|}{|\mathcal{N}_h|} \right) = \frac{1}{2} \left(\frac{|\mathcal{N}_{h,(1,0)}|}{|\mathcal{N}_{h,(1,0)}| + |\mathcal{N}_{h,(1,1)}|} \right) \quad (4)$$

Intuitively, this estimator represents the strength of the spatial relationship, which can be estimated as the ratio of 1–0 pairs to the total number of pairs in that binned interval. Visually, this is shown in Figure 3b,d,e, where the empirical estimates (black dots) correspond to half the ratio of the grey bar height to the combined height of the grey and blue bars. The empirical estimates close to 0.5 indicate weak or no spatial relationship between EPEs recorded at stations in the neighbourhood, whereas smaller values denote a stronger spatial relationship.

Figure 3a–d illustrate semivariogram estimation for two individual days. To ensure more robust estimation, here we focus on estimation of a climatological semivariogram $\hat{\gamma}_{\text{season}}(h)$ based on all EPEs within a given season. To obtain climatological length scales, we grouped all 1–1 pairs and 1–0 pairs within each station's 500-km neighbourhood based on the bin interval $(h - \delta, h]$, pooling across all EPE days (d) within a given season from 1940 to 2024:

$$\hat{\gamma}_{\text{season}}\left(h - \frac{\delta}{2}\right) = \frac{1}{2} \left(\frac{\sum_{d \in D} |\mathcal{N}_{h,(1,0)}^{(d)}|}{\sum_{d \in D} |\mathcal{N}_h^{(d)}|} \right) = \frac{1}{2} \left(\frac{\sum_{d \in D} |\mathcal{N}_{h,(1,0)}^{(d)}|}{|\mathcal{N}_{h,(1,0)}^{(d)}| + |\mathcal{N}_{h,(1,1)}^{(d)}|} \right) \quad (5)$$

where D is the set of EPE days for the season of interest. This process is illustrated in Figure 3e. The same procedure was applied to estimate spatial scales of EPEs associated with ENSO in each season (see Section 2.3).

For this estimator to be robust, we required each station to have at least 20 neighbours within its 500-km neighbourhood, excluding 14 stations that did not meet this criterion. We further retained only EPE days where at least 10% of neighbourhood stations exceeded P90, thereby filtering out events detected by only one or two stations. A sensitivity test without this filter yielded similar overall results, but isolated-station events lacked sufficient spatial coherence for reliable scale estimation.

The semivariogram in this form (Equations 4 and 5) does not reveal the spatial scale of EPEs. To estimate the spatial scale of EPEs, we next fit a parametric model to the semivariogram estimate $\hat{\gamma}(h)$ as described below.

2.2.3 | Estimating Semivariogram Parameters

Various theoretical semivariogram models can be used to model spatial autocorrelation (Webster and Oliver 2007; Cressie 2015). For example, Touma et al. (2018) and Tan et al. (2021) used the exponential model, while Touma et al. (2019) adopted the spherical model. Using synthetic data, we compared exponential and spherical fits, finding heuristically that the spherical model was less sensitive to changes in station coverage and exhibited less bias than the exponential model. Based on this, we adopt the spherical model for semivariogram fitting and leave it to future work to investigate parametric model selection further. The spherical semivariogram is given by

$$\gamma(h) = \begin{cases} 0, & h=0 \\ c+b \frac{3h}{2\alpha} - \frac{1}{2} \left(\frac{h}{\alpha}\right)^3, & 0 < h \leq \alpha \\ c+b, & h \geq \alpha \end{cases} \quad (6)$$

where c , b , and α are the nugget, the partial sill, and the length scale of the semivariogram, respectively (Cressie 2015). The nugget c accounts for variability at very short distances. The nugget and partial sill determine the sill ($b + c$), which is the $\gamma(h)$ value approached by the spherical semivariogram at large separation distances. The length scale α is the separation distance at which the semivariogram levels off, indicating the distance beyond which spatial proximity no longer governs the semivariogram (red dashed lines in Figure 3b,d,e). Following Touma et al. (2018), we use the length scale α of $\hat{\gamma}_{\text{season}}$ to represent the climatological spatial scale of EPEs. The fitted semivariogram was calculated using the GSTools package with the Python programming language (Müller et al. 2022).

2.3 | ENSO Events Classification and Bootstrapping

To identify ENSO EPEs, we use the five-month rolling mean Southern Oscillation Index (SOI). The SOI is based on the standardised anomaly of the mean sea-level pressure differences between Tahiti and Darwin, with records available from January 1876 (Trenberth 1984). Sustained negative SOI values below -7 are typically associated with El Niño conditions, while sustained positive values above 7 indicate La Niña conditions.

To ensure adequate and comparable samples for semivariogram estimation, stations must record at least 20 EPEs in both ENSO phases within a season. Thus, only stations with ≥ 20 El Niño and ≥ 20 La Niña events per season are retained (e.g., a station with 5 El Niño and 30 La Niña events in SON is excluded). To have sufficient stations meet this criterion, the SOI threshold was relaxed from ± 7 to ± 5 . The EPEs are then classified by their 5-monthly SOI with $\text{SOI} > 5$ as La Niña and $\text{SOI} < -5$ as El Niño. After relaxing the SOI thresholds, 3115 out of the total 9861 stations meet the minimum event number requirement in at least one season. Stations that do not meet this requirement are primarily those with shorter data records and/or located in remote areas, where limited observations make the ENSO response appear weak or inconsistent (not shown). The semivariogram estimation was done using all 9861 available neighbour stations with 500-km neighbourhoods centred at these 3115 stations.

To quantify uncertainty in the estimated length scales, we applied bootstrapping separately for each ENSO phase and season at each station. While various bootstrapping methods are available (see e.g., Paciorek et al. 2018, and citations therein), we used the basic bootstrap for simplicity. To equalise sample sizes between phases, the number of events used in bootstrapping was set to the smaller of the two phases within a given season. For example, if a station had 60 La Niña and 90 El Niño events in DJF, we first ranked the 90 El Niño events by the absolute 5-month rolling mean SOI and

then subsampled 60 events evenly across the ranked distribution, thereby preserving coverage across the SOI range. For both phases, the 60 events were then resampled with replacement for bootstrapping. The with-replacement sampling was repeated 1000 times. For each bootstrap sample, the semivariogram approach was applied to estimate the climatological length scale, producing distributions of length scales for El Niño and La Niña events, as well as their differences (La Niña minus El Niño).

To compare EPE length scales between ENSO phases, we used the differences in the median values of their respective bootstrap samples. Statistical significance was assessed at the 90% confidence level based on bootstrap distributions. We consider differences in the median statistically significant if at least 90% of the bootstrap samples are on the same side of zero as the differences in the median. More specifically, significance is assigned when:

- The differences in the median and the 10th percentile of the 1000 sample differences are both positive or
- The differences in the median and the 90th percentile of the 1000 sample differences are both negative.

2.4 | Trend Analysis Using Long-Term Rain Gauge Records

The long time coverage of the data used in this study naturally raises the question of how the length scales of EPEs change over time. Unfortunately, the number of active BoM stations varies over time, with many stations being decommissioned and new stations coming online (see Figure S1). Only 1705 stations in Australia have been continuously operating from 1940 to 2024, and only a few of these stations have enough neighbour stations with comparable long-term records for semivariogram analysis. Therefore, for the trend analysis, we only present the climatological length scales of EPEs for the 500-km neighbourhood centred at the 2070 stations that have been operating from 1st January 1960 to 31st December 2023, which we refer to as “long-term stations” (locations see Figure S3). This is to balance the need between the spatial coverage and the length of the record. The climatological length scale results for the long-term stations generally agree with those for the 9861 stations presented below (see Figure S4).

For the trend analysis, we first divided the period between 1960 and 2023 into two halves: 1960–1991 and 1992–2023. Then, we estimated the climatological length scales separately for the two periods for each long-term station. Finally, we compared the climatological length scales for each season between the two periods to assess how the EPE length scales change over time.

3 | Results

3.1 | Seasonal Length Scale of EPEs

Figure 4 shows the seasonal climatology of EPE length scales, and Figure 5 summarises these results based on NRM regions. For reference, we present the number of EPEs used in

the semivariogram estimation at each station in each season in Figure 6. We will describe the seasonal and regional variation in length scale in more detail below; here we note that these seasonal and regional patterns are coherent, and they do not simply mirror those of P90 thresholds (Figure 2) or mean precipitation (Figure S2).

We assessed the statistical significance of seasonal variations within each NRM region using the paired Wilcoxon signed-rank test (Wilcoxon 1945), and seasonal differences between NRM regions using the Mann–Whitney U test (Mann and Whitney 1947), following approaches similar to Touma et al. (2018) and Tan et al. (2021). These tests were used to evaluate whether median EPE length scales differ significantly across seasons or between regions. The computation of the paired Wilcoxon signed-rank test, Mann–Whitney U test, and p values is conducted using the SciPy package (Virtanen et al. 2020). Results of statistical significance tests for the intraseasonal and intraregional differences are shown in Figures 7 and 8, respectively.

3.1.1 | Intraseasonal Comparison

Seasonal differences in EPE length scales across Australia's 15 NRM regions reflect the continent's climatic diversity (Figure 7). Most regions exhibit a seasonal cycle with seasonal changes of less than 100 km in spatial extent.

The monsoon-impacted tropical regions (Monsoon North West, Monsoon North East, Wet Tropics) and adjacent East Coast North present a notable paradox: while the number of EPEs is lowest during the dry season (JJA and SON; Figure 6), the median length scales are at their largest (Figure 5a–c). This reflects the influences of the monsoon. During the wet season (November to April), rainfall is dominated by localised convective systems that are usually smaller in size (e.g., Pope et al. 2008; Jackson et al. 2018), whereas in the dry season, when EPEs are less frequent, the associated P90 thresholds are also lower (Figure 2). Consequently, a storm with a given physical footprint and intensity will exceed the P90 threshold at more stations in the dry season, making its estimated length scale appear larger than an equivalent storm in the wet season. These dry season events are classified as extremes only when seasonal P90 thresholds are applied. Note that fewer than 10 EPEs were recorded at stations in Monsoon North West during JJA (brown grid boxes in Figure 6). Our sensitivity test (see Figure S5) showed that a low sample size, especially lower than 20, may lead to inaccurate estimates of the climatological length scale shown in Figure 5. We present the results for low EPE numbers for completeness, but any interpretation should account for the potential inaccuracies associated with the small sample size.

In the eastern regions, Rangeland East and East Coast North exhibit the largest median climatological length scale in JJA (Figure 5e,f), while East Coast South and Central Slope show the largest median climatological length scale in DJF (Figure 5f,i). In the western regions (Southern Flatlands West and Rangeland West), both EPE frequency and length scale peak during JJA (Figure 5d,g; Figure 6), coinciding with enhanced frontal precipitation in this season (Prescott et al. 1952; Pook et al. 2012; Raut et al. 2014).

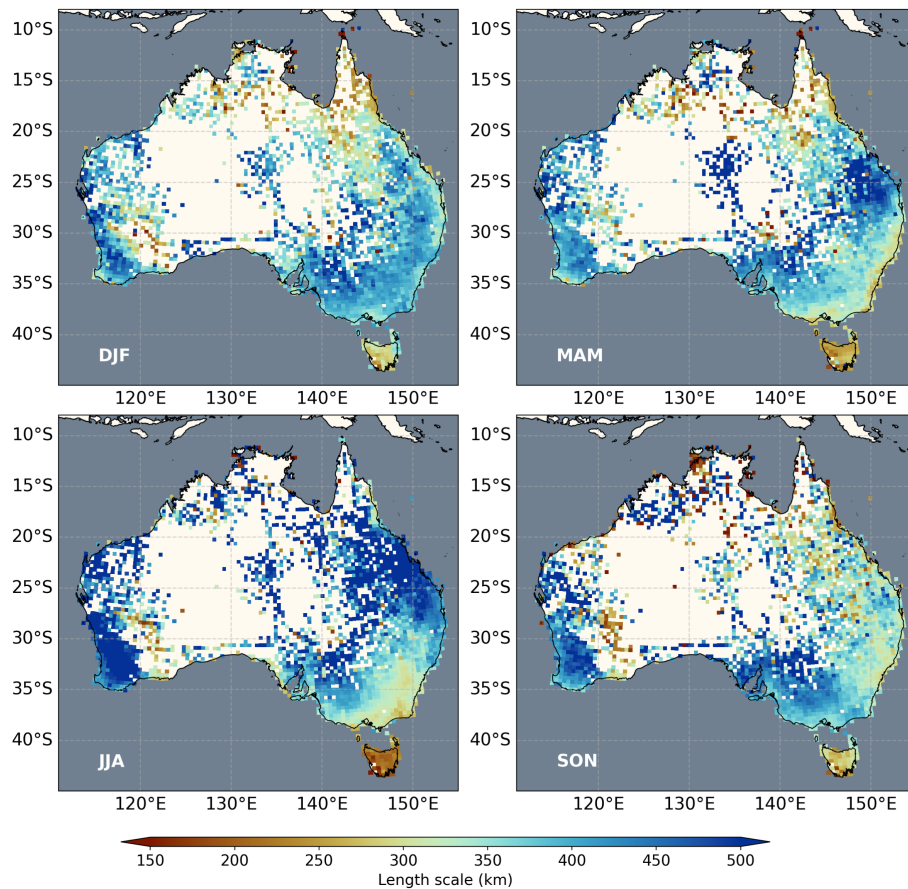


FIGURE 4 | Seasonality of the climatological length scale of EPEs based on 40-km gridded station averages.

The southern regions (Southern Flatlands East, Tasmania West, Tasmania East, Murray Basin, Victoria West, and Victoria East) generally show a greater number of EPEs in JJA (Figure 6) and a larger climatological length scale in DJF and SON (Figure 5h–o). Although JJA features the highest number of extreme-day exceedances in southern regions (Figure 6), the associated P90 thresholds are lower (Figure 2) and the spatial length scales are smaller (Figure 4). This pattern does not necessarily imply a dominance of frontal events, as the analysis of Pepler et al. (2020) shows no substantial frontal contribution to EPEs in these regions. Instead, this likely reflects the high frequency of diverse, moderate-intensity precipitation systems during JJA in the southeast, which exhibit limited spatial coherence. These regional contrasts in frontal influence suggest that the processes controlling the spatial scales of EPEs vary regionally across Australia.

3.1.2 | Intraregional Comparison

To aid the interpretation of spatial patterns of EPE length scales, we added a full-record scale analysis. Rather than defining EPEs separately by season, we computed the P90 thresholds over the entire analysis period for each station and then estimated EPE length scales for the full period using the same semivariogram workflow described in Section 2.2. The resulting median length scales for each NRM region are shown in Figure 9. Here,

hexagonal maps were used to reduce visual bias from the large area extent of central Australia. This full-record view provides an integrated, regionally comparable image that characterises the most extreme days, complementing the seasonal panels.

Most regional differences in median length scales are highly significant ($p < 0.01$; Figure 8), confirming that these are robust patterns rather than random chance. The full-record climatology highlights broad and persistent regional contrasts in the spatial extent of extreme precipitation across Australia. Figure 9a shows that length scales are largest over the western and central regions, and smallest over Tasmania and the tropical north. Seasonal analysis (Figure 9b–e) illustrates a similar pattern with western regions (Southern Flatlands West and Rangeland West) consistently larger than other regions. The spatial contrast is most pronounced in JJA, when variability across the continent is greatest and strongly significant ($p < 0.01$; Figure 8d).

Tropical regions (Monsoon North West, Monsoon North East, and Wet Tropics) display smaller EPE length scales than most other areas in both the long-term and seasonal analysis, with the exception of JJA, when the limited number of events leads to higher uncertainty (Figure 9). This agrees with the fact that tropical regions receive most of the precipitation during their wet season associated with more frequent and localised convective activity (Pope et al. 2008; Jackson et al. 2018; Bowden et al. 2025).

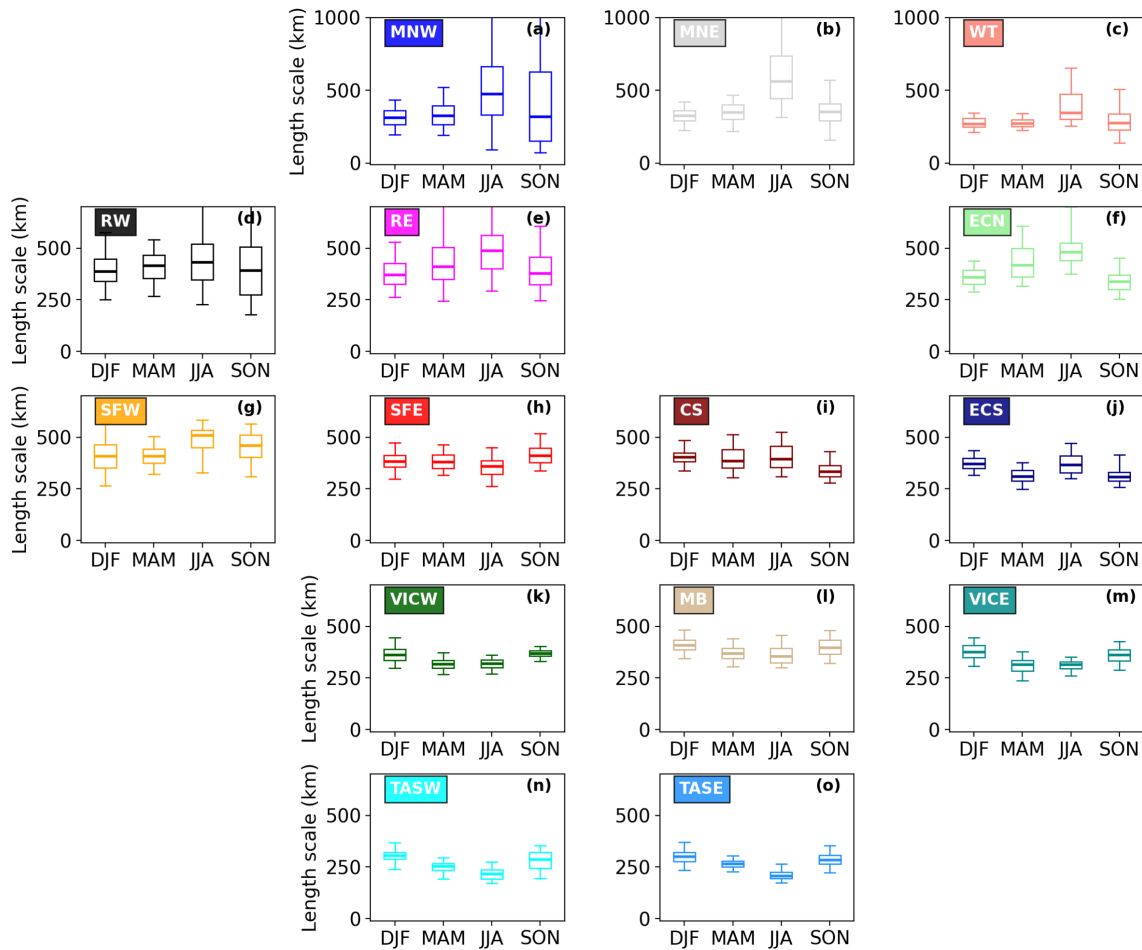


FIGURE 5 | Box plots showing the seasonal length scales of EPEs for stations grouped by NRM regions. Boxes span the 25th–75th percentiles, with the centre line marking the median, and whiskers extending from the 5th to the 95th percentiles. Seasons are shown on the x-axis and estimated length scales on the y-axis, with subplots corresponding to NRM regions. The y-axis is consistent across subplots to enable direct comparison, except for the top row, which shows results for NRM regions in northern Australia. In these regions, higher uncertainty and lower confidence in some estimates arise from low event numbers (< 10; see Figure 6) and sparse station coverage.

Tasmania (TASW and TASE) shows the smallest climatological length scales of any region (Figures 4 and 9). The overall pattern of small length scales is not fully attributable to Tasmania's isolation from the mainland. The number of available stations at the distance beyond the size of Tasmania (> 300 km) is comparable to that of many mainland regions. Rather, the small length scales likely reflect genuine spatial variability associated with the large scale circulation and weather systems impacting southeastern Australia. In nearby regions (Victoria West and Victoria East), the EPE length scales are also smaller than other coastal regions to the north (e.g., East Coast North), especially in JJA. A sensitivity test using neighbourhood radii of 300 and 700 km (not shown) further confirmed that these short length scales are not an artefact of the 500-km radius; they remained consistently smaller than those on the Australian mainland across all test cases.

Another plausible factor contributing to the small EPE length scales in Tasmania is its complex topography. The presence of mountain ranges leads to a strong west–east rainfall gradient (see figure 1 in Tozer et al. 2018), making it uncommon for an EPE to simultaneously exceed extreme thresholds on both sides of the island, naturally limiting the spatial coherence of EPEs. A

similar topographic effect is evident along the east coast of the mainland, where in MAM the EPE length scales are relatively small (Figure 4) despite higher event counts (Figure 6), while stations west of the Great Dividing Range experience fewer EPEs (Figure 6).

One may notice very low values shown in some of the pixels in Tasmania in Figure 4. These are caused by a few stations with unusually small estimated length scales located in areas with low local station density. These stations are treated as outliers and are therefore not presented in the regional boxplots (Figure 5). When interpolated to a 40-km grid, the influence of such stations becomes visually amplified, producing the appearance of localised low-value pixels. Regardless of the plotting artefact, the reduced length scales observed in both Tasmania and the tropical regions are consistent with the findings of the global study by Tan et al. (2021).

3.2 | Seasonal Length Scales of ENSO Events

Figures 10, 11, and 12 show the seasonal length scales of EPEs for El Niño and La Niña conditions, along with their differences

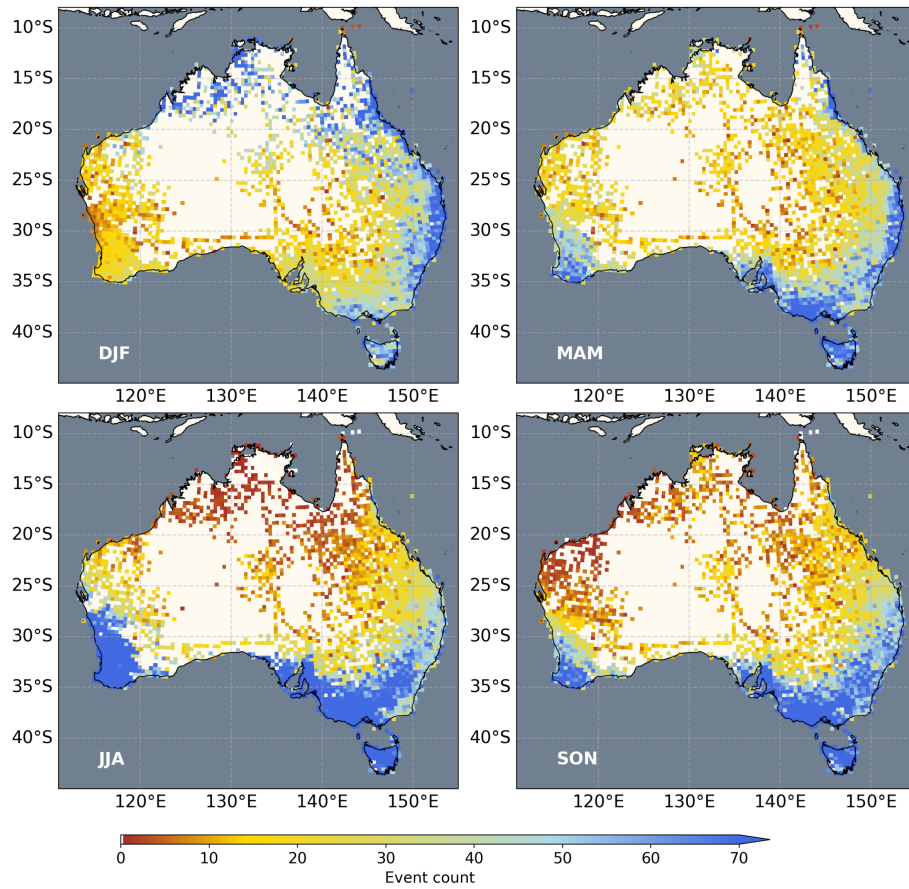


FIGURE 6 | Maps similar to Figure 4, but showing the number of EPEs included at each station in the climatological length scale analysis from 1940 to 2024.

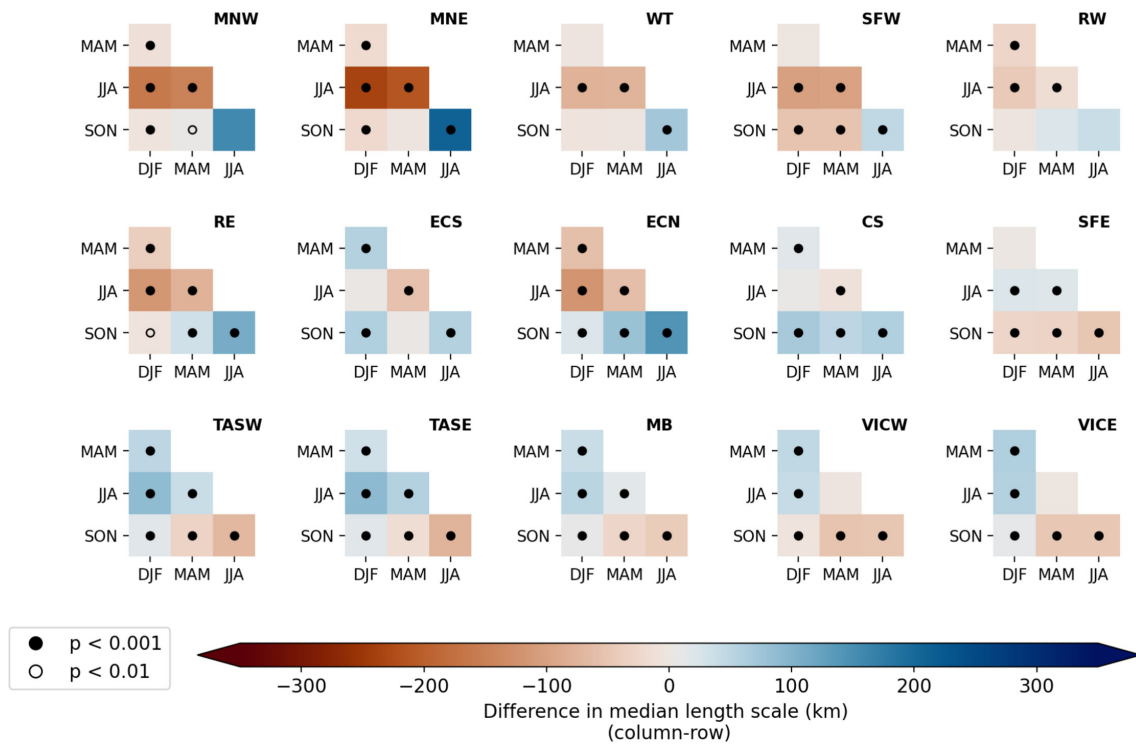


FIGURE 7 | Heatmap showing magnitude and significance of the intraseasonal differences in the median seasonal length scales of the EPEs using the paired Wilcoxon signed-rank test. The shading of each box represents the differences in the median length scale of the column season minus that of the row season. The marker inside each box illustrates the significance level of the paired Wilcoxon signed-rank test as shown in the legend.

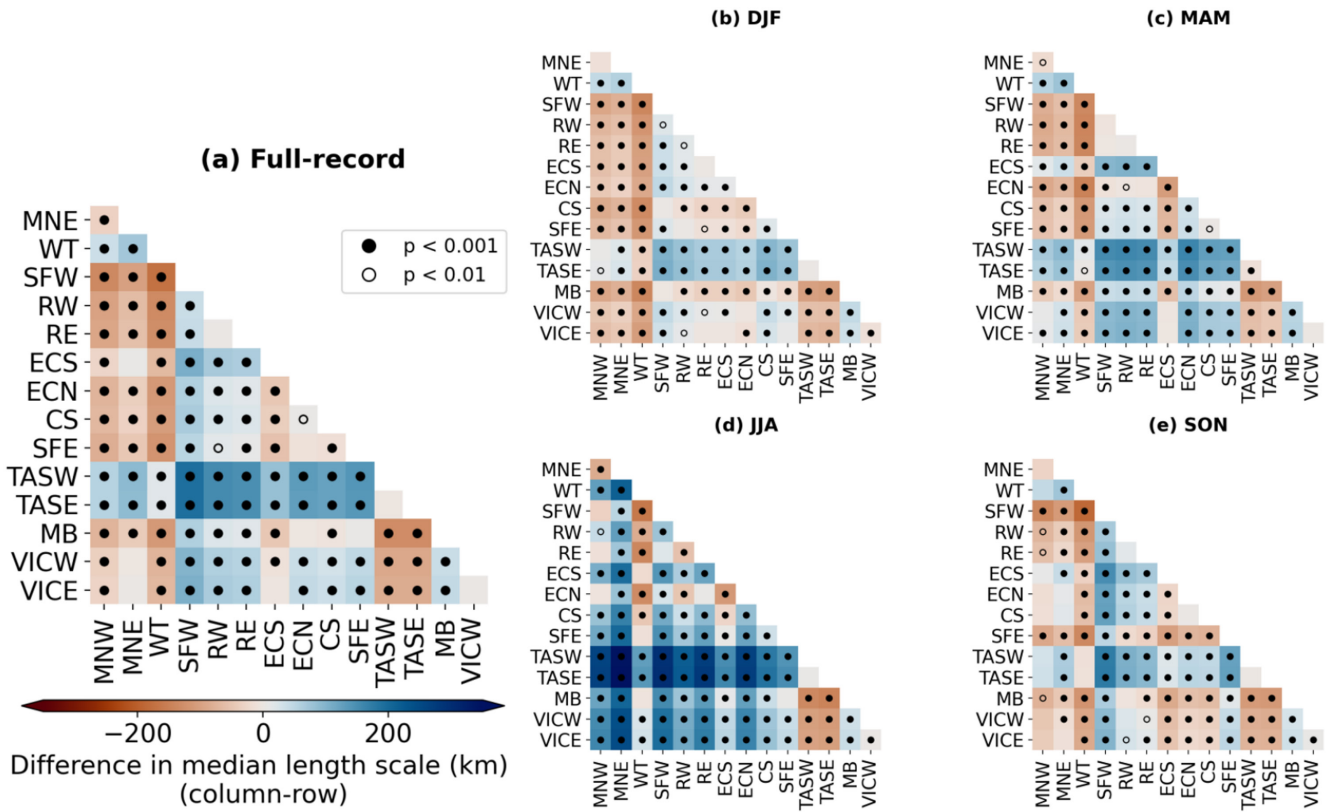


FIGURE 8 | Similar to Figure 7, but for the magnitude and significance of the intraregional differences in the median length scales for full-record scale EPEs (a) and each season (b–e) using the Mann–Whitney U test.

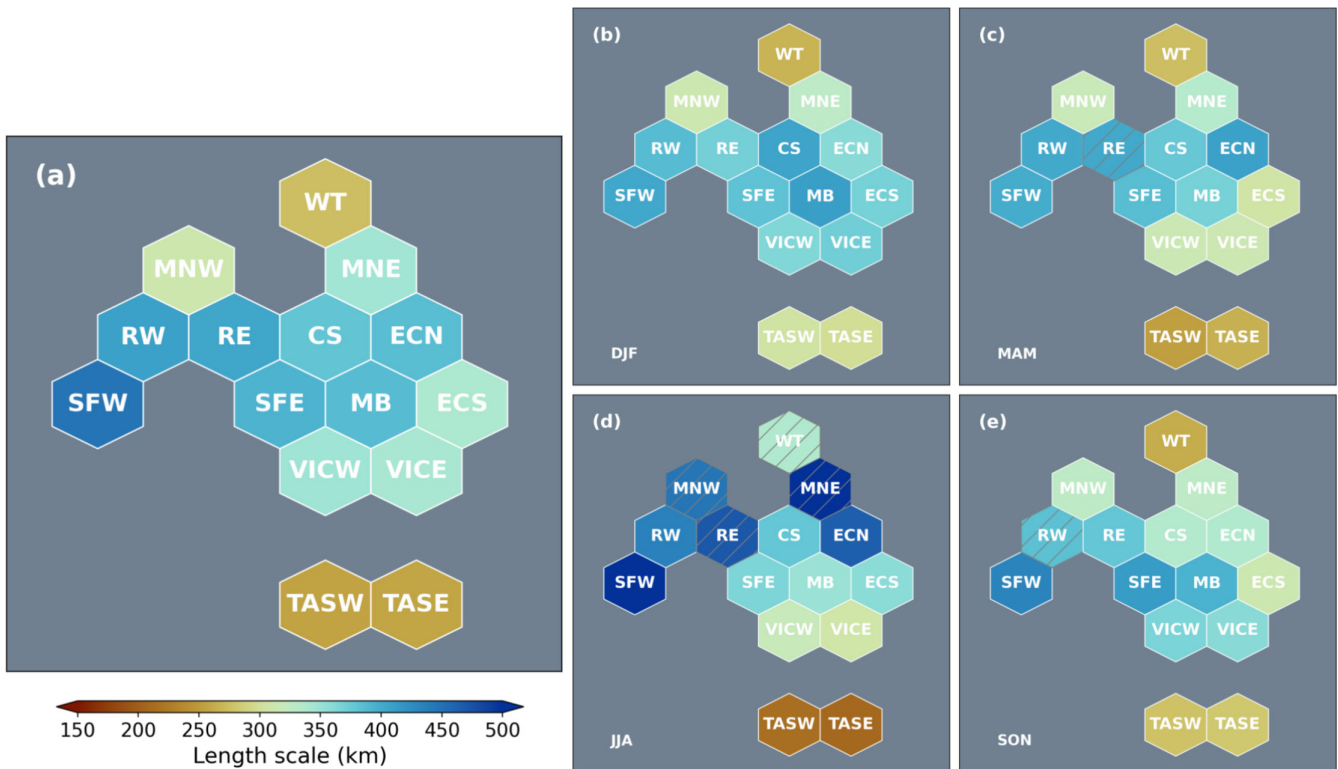


FIGURE 9 | Hexagonal maps showing the median length scales for full-record scale EPEs (a) and each season (b–e) for each NRM region. Hexagonal cells with grey hatching indicate regions with low confidence in the estimated length scale due to a low number of EPEs (see Figure 6).

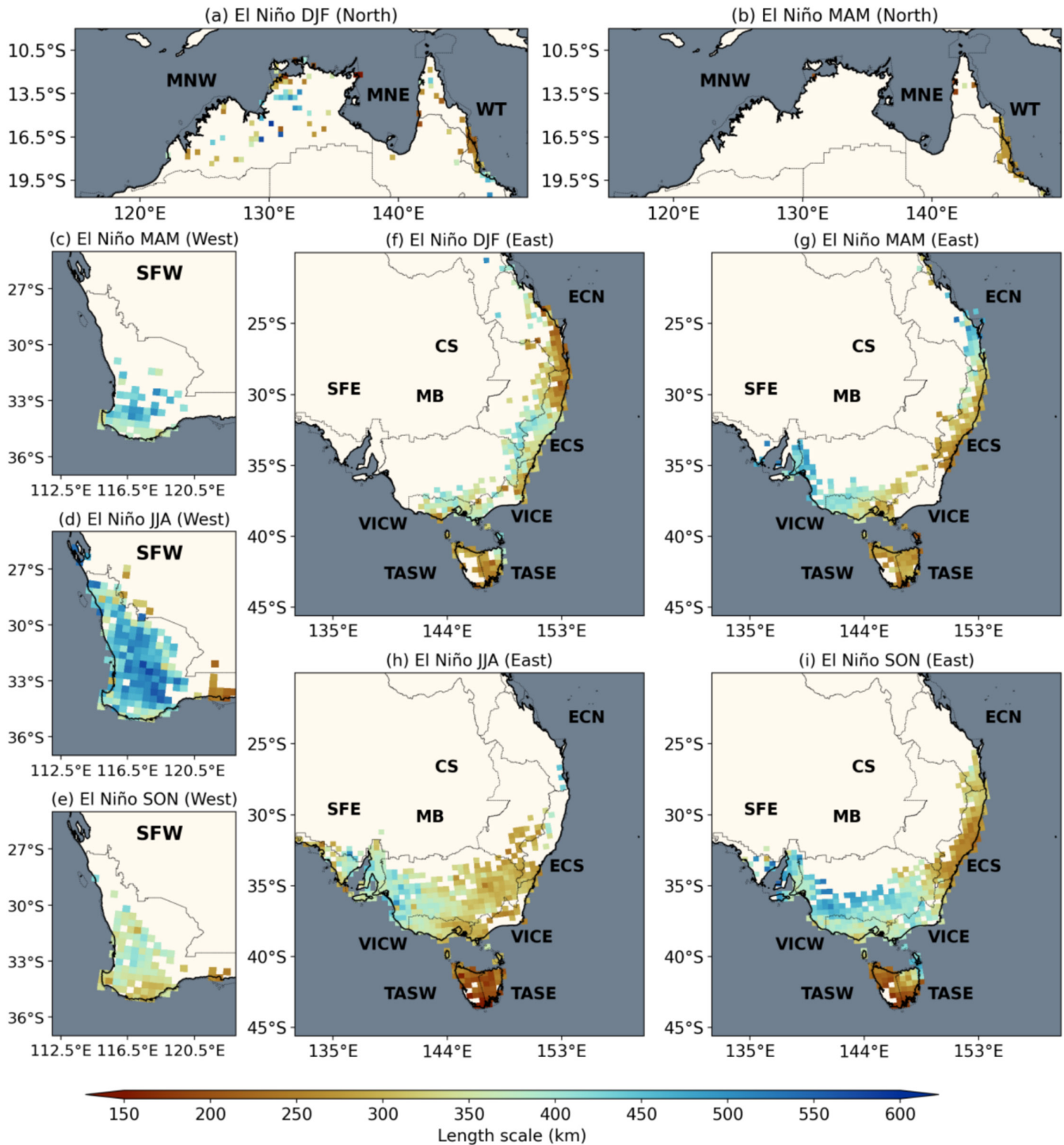


FIGURE 10 | Maps illustrating the climatological length scale for El Niño in northern (a, b), southwestern (c–e), and southeastern (f–i) regions. The displayed values are median length scales of 1000 bootstrap iterations for each station. Results for JJA and SON in the northern regions and DJF in SFW are not displayed due to insufficient ENSO events at stations in these regions.

at each station (La Niña length scale minus El Niño length scale). The displayed results show the median length scales of 1000 bootstrap samples for both ENSO phases. Details of the number of stations included for each NRM region and season, as well as the number of statistically significant cases, are provided in Table S1. At several stations, the differences in EPE length scales between ENSO phases are statistically significant at the 90% confidence level, indicating that these differences are unlikely to be due to random variability. Since

several NRM regions have fewer than 10 stations in certain seasons, we only present the analysis for seasons and regions with sufficient stations. Rangeland West and Rangeland East in all seasons, Southern Flatlands West in DJF, and northern regions (MNW, MNE, and WT) in JJA and SON are therefore excluded. Note that Monsoon North East in DJF and MAM, Monsoon North West in MAM (Figures 10b, 11a, and 12b), Southern Flatlands East in DJF (Figures 10f, 11a, and 12f), Victoria East and Central Slope in MAM (Figures 10g, 11a,

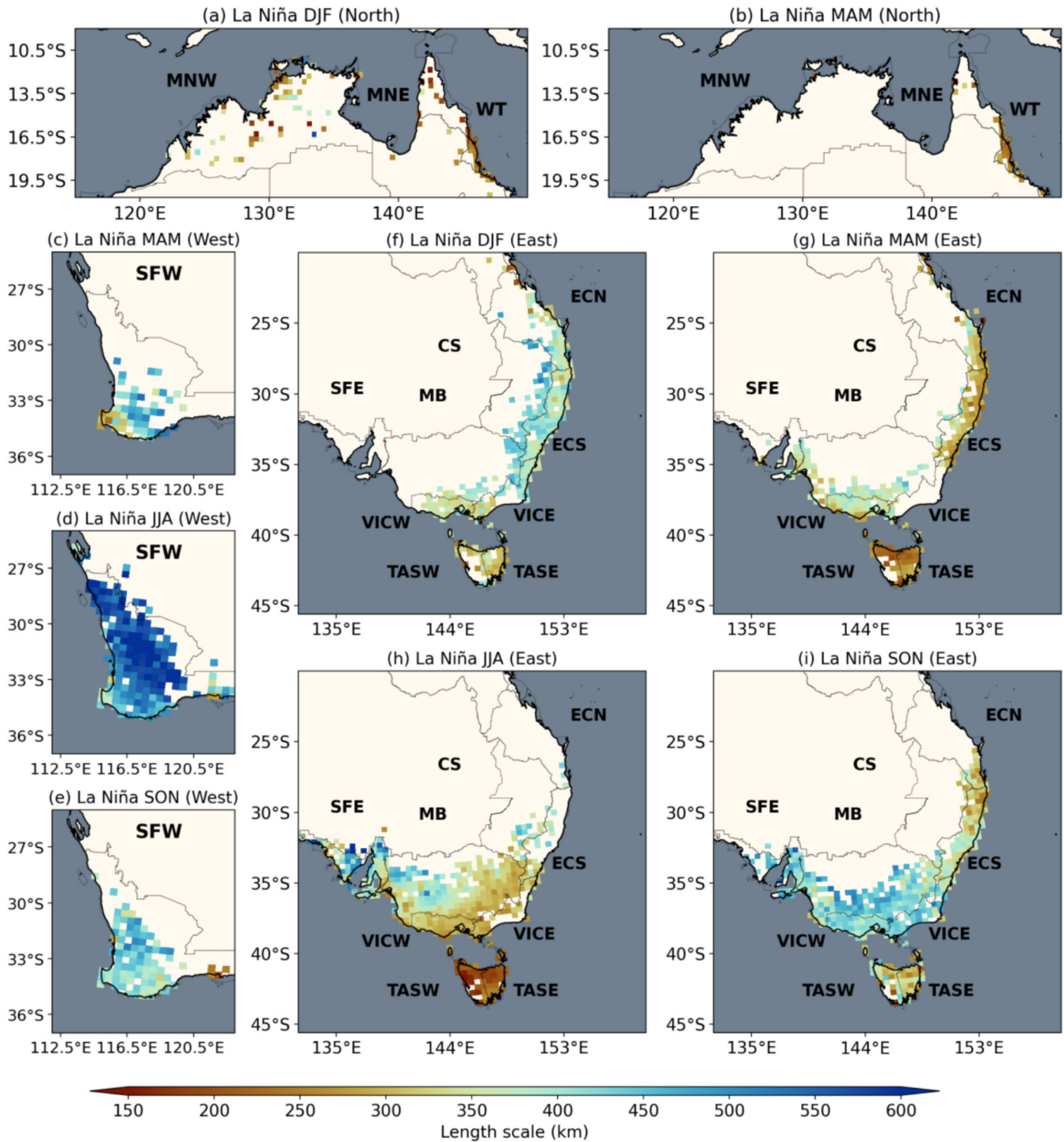


FIGURE 11 | Same as Figure 10, but for La Niña.

and 12g) and East Coast North in JJA (Figures 10h, 11a, and 12h) include fewer than 20 stations. Caution should be exercised when interpreting these results.

While La Niña episodes are usually associated with wetter conditions than El Niño in eastern Australia with respect to both mean and extreme precipitation (e.g., Nicholls et al. 1997; Risbey et al. 2009; King et al. 2014), the differences in EPE length scales between the two ENSO phases still exhibit strong seasonality and vary across regions. In eastern Australia, East Coast North and East Coast South exhibit more stations with larger

EPE length scales during La Niña in DJF (Figure 12f), with East Coast North showing the opposite in MAM (Figure 12g). Moving to JJA and SON, stations in East Coast South still show more stations with a larger EPE length scale associated with La Niña (Figure 12h,i), while East Coast North does not show a clear response of EPE length scale to ENSO in SON.

The seasonality in Tasmania East is similar to that in East Coast North, with La Niña linked to a smaller EPE length scale for the majority of stations in MAM only (Figure 12g). Tasmania West presents the opposite to Tasmania East during JJA, with

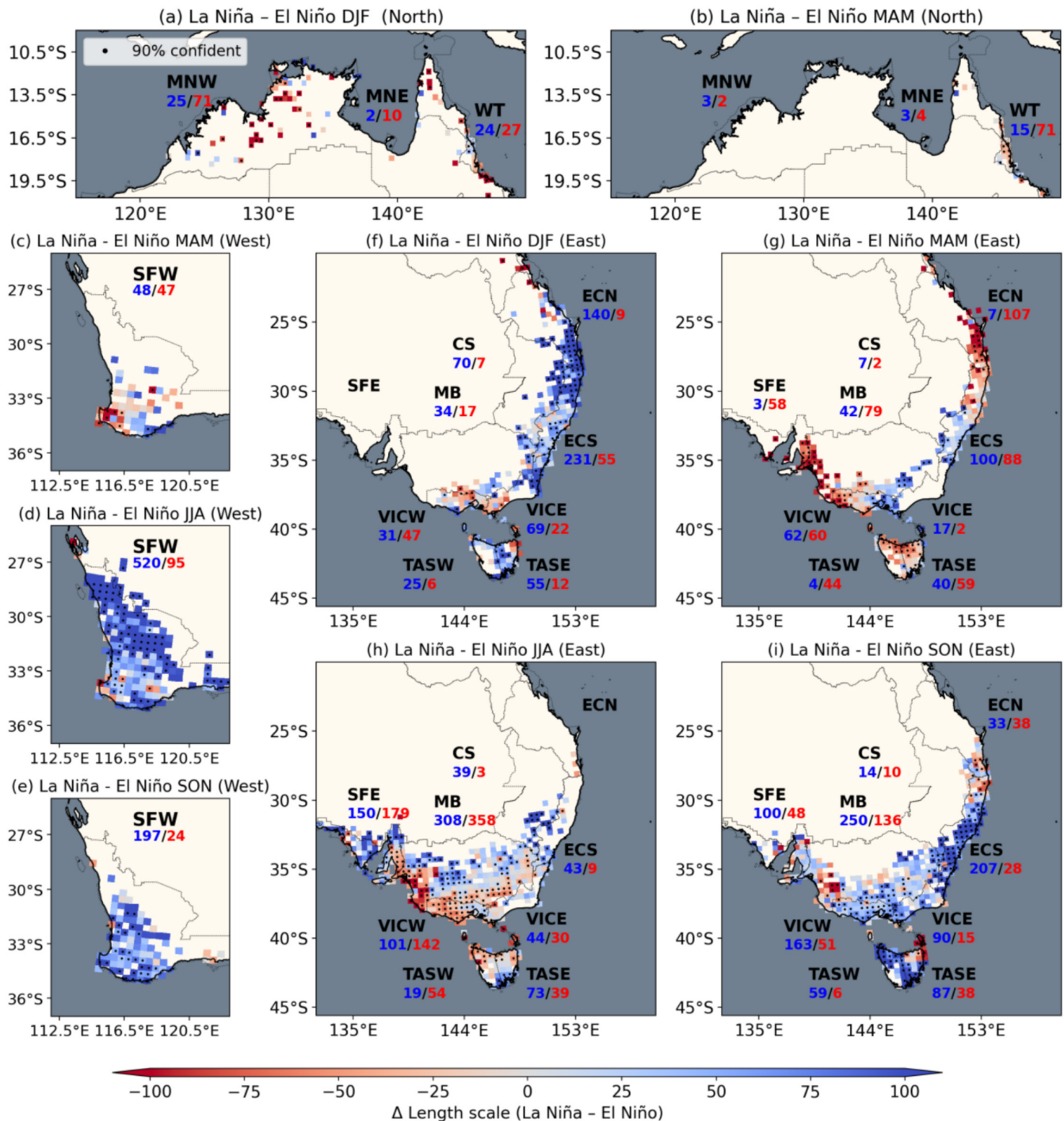


FIGURE 12 | Same as Figure 10, but the difference in median length scale between La Niña and El Niño. Each panel also indicates the number of stations with larger EPE length scales during La Niña (blue) and El Niño (red). Stippling with black dots indicates grid boxes that contain at least one station exceeding the 90% confidence level. For more details of the station statistics for each region and season, see Table S1.

more stations showing a larger EPE length scale during El Niño (Figure 12h). A similar west–east contrast can be seen in Victoria West and Victoria East in JJA in which the EPE length scale during La Niña is larger in the east but smaller in the west for most stations (Figure 12h). Moving further inland, Central Slope exhibits a larger EPE length scale during La Niña for most stations in all seasons, while Murray Basin and Southern Flatlands East show more stations associated with larger EPE length scales during El Niño for MAM and JJA (Figure 12g,h).

In southwestern Australia (Southern Flatlands West; Figure 12c–e), the majority of stations display larger EPE length scales during La Niña compared to El Niño in MAM, JJA, and SON. One exception is south Southern Flatlands West in MAM, where most stations show El Niño coincides with larger EPE length scales. In northern Australia, only a small number of stations have sufficient samples, but most stations show smaller EPE length scales during La Niña compared to El Niño in DJF (Figure 12a). This pattern is also observed in Wet Tropics in

MAM (Figure 12b). To ensure the robustness of our analysis, we verified that the selected ENSO events are not dominated by any single year (i.e., an El Niño or La Niña event that is particularly dry or wet) and that, consistent with established patterns, most stations coincide with higher seasonal total and mean precipitation in each La Niña year.

To provide additional insight into the underlying rainfall regimes across Australia, we also examined the relationship between ENSO-related differences in EPE spatial scale and the corresponding differences in the P90 thresholds and mean rainfall (Figures S6 and S7). These bivariate choropleth maps show that in general, changes in EPE length scales between ENSO phases do not have a strong relationship to changes in the magnitude of EPEs or the mean rainfall. This weak relationship is also reflected in the overall correlation between ENSO-related changes in length scale and rainfall (~ -0.23 when evaluated across all stations and seasons; not shown). Exceptions are found along the East Coast (ECN and ECS) during DJF and across eastern and southeastern Australia during SON. The latter corresponds to where ENSO–rainfall correlations are known to be the strongest (e.g., Chung and Power 2017; Risbey et al. 2009; Gillett et al. 2023).

Locations showing both larger EPE length scales and higher rainfall during El Niño (red pixels in Figures S6 and S7) are fewer than those exhibiting the same pattern during La Niña (dark blue pixels in Figures S6 and S7). One may interpret this asymmetry as indicating that La Niña tends to enhance not only rainfall intensity but also the spatial extent of EPEs. While this pattern is true for DJF and SON in eastern and southeastern Australia, it no longer holds in MAM and JJA in the same regions, where increases in rainfall amount (both mean and P90) do not correspond to larger EPEs during La Niña (yellow pixels in Figures S6g–h and S7g–h). Although the weaker ENSO–rainfall relationship during MAM may partly contribute to this decoupling, it does not explain the contrasting behaviour in JJA, when ENSO's influence on rainfall is relatively strong (e.g., see figure 2 in Risbey et al. 2009). These results suggest that La Niña or El Niño may increase the mean rainfall without necessarily broadening the spatial footprint of heavy precipitation, indicating that changes in rainfall amount and spatial scales are not always linearly coupled. The local synoptic systems may play a greater role in modulating the spatial scales of EPEs. Understanding the mechanisms that drive contrasting responses of EPE intensity and EPE length scale to ENSO variations is therefore an important avenue for future research.

3.3 | Long-Term Trends in the Seasonal Length Scales

Figure 13 compares the differences of the median values of EPE length scales for each NRM region between 1960–1991 and 1992–2023. The statistical significance of the differences is evaluated using the Mann–Whitney U test. More details of the seasonal length scales in each NRM region are shown in the boxplots and maps in Figures S8 and S9, respectively. Here, we focus primarily on the long-term changes in the medians of climatological length scale in each NRM region. The long-term

changes in the mean rainfall and P90 thresholds are shown in Figures S10 and S11, respectively.

Only southwestern Australia (Southern Flatlands West) and most regions in the east and southeast (East Coast South, East Coast North, Central Slope, Southern Flatlands East, Tasmania East, Murray Basin, Victoria West, and Victoria East) have a good spatial coverage of stations (Figure S3). Therefore, we mainly focus on these regions for the trends in the climatological length scale. DJF results for Southern Flatlands West are omitted because the total number of EPEs is already low in the full analysis (Figure 6), and splitting the period yields insufficient events for a meaningful comparison. As changes in rain gauge network density may affect length scale estimates, we present results based solely on the 2070 long-term stations here. We conducted the same analysis that includes all 9861 neighbour stations within neighbourhoods centred on the long-term stations. The results from both the long-term and 9861 neighbour station sets are largely consistent (not shown).

The trend analysis of EPE length scales reveals geographically coherent patterns across Australia, with most of the observed changes being statistically significant (Figure 13). A notable increasing trend is seen across the southern and southeastern regions (Murray Basin, Victoria West, and Victoria East) during SON, while a decreasing trend is common in MAM. The Tasmanian regions (TASW and TASE) share a similar trend of decreasing in DJF and JJA, and increasing in MAM and SON. East Coast South exhibits a decreasing trend in all seasons. Further west, Southern Flatlands East shows an increase in all seasons except JJA, while Southern Flatlands West exhibits a general decreasing trend.

Southern and southeastern Australia experienced the prolonged “Millennium Drought” before 2010 (Van Dijk et al. 2013). To assess its influence, we repeated the trend analysis using two drought-excluded periods (1960–1973 and 2010–2023). To maintain readability and avoid overcomplicating Figure 13, the drought-excluded analysis is not shown. The results, however, are largely consistent with the main analysis. Only a few region–season combinations show the trend reverses to statistically significant increases in length scale once the drought years are omitted (Central Slopes in SON; East Coast South in SON; East Coast North in MAM and SON; Victoria West in MAM; Victoria East in DJF).

The above patterns in changes to the length scale of EPEs do not typically correspond to those in mean precipitation (Figures S11 and S12) or in the P90 thresholds (Figures 13 and S10). Correlations between changes in EPE length scale and rainfall amount (both mean and P90) are weak (within the range of ± 0.3 ; not shown) in most regions and seasons. There are two notable exceptions. First, the strong reduction in EPE length scales in Southern Flatlands West aligns with a documented drying trend in southwestern Australia (Dey et al. 2019; CSIRO and Bureau of Meteorology 2024), particularly reflected in the decreases in the P90 threshold in JJA (Figure 13c) and in mean rainfall in JJA and MAM (Figure S12), matching the long-term April–October rainfall decline reported by CSIRO and Bureau of Meteorology (2024).

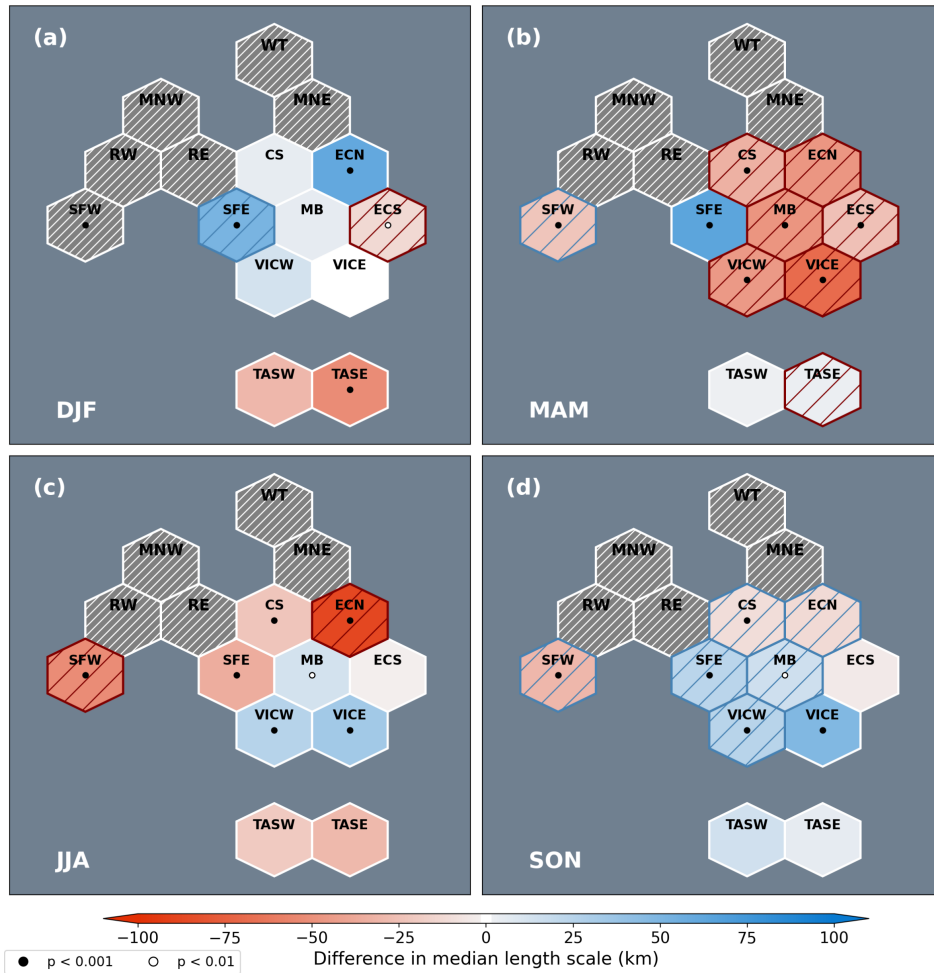


FIGURE 13 | Hexagonal maps showing magnitude and significance of the differences in the median seasonal length scales of the EPEs for each NRM region using the Mann–Whitney U test for DJF (a), MAM (b), JJA (c), and SON (d). The shading of each region represents the differences of the median values in 1992–2023 minus those of 1960–1991 with blue (red) denoting increases (decreases). Values within ± 10 km are shown in white. Circle markers at region centroids illustrate the p values of the Mann–Whitney U test. Hatched hexagons highlight regions with statistically significant increases (blue) or decreases (red) in the median P90 thresholds. Results for DJF in SFW, and all seasons in MNW, MNE, WT, RW, and RE are not shown due to insufficient number of EPEs and/or stations.

Second, the median EPE length scales, P90 thresholds, and mean precipitation all exhibit decreasing trends during MAM across southeastern and eastern Australia (Victoria West and East, Tasmania West and East, Murray Basin, Central Slope, and East Coast South and North; Figure 13b). In these same regions, the increasing trend in the P90 thresholds in SON is consistent with their counterparts in EPE length scales, especially after the removal of the Millennium Drought (not shown). Notwithstanding the regions mentioned here, it is clear that the overall trends in EPE length scale are not directly related to trends in mean precipitation or EPE intensity. This again highlights a need to understand the different mechanisms that set the size of EPEs in addition to their intensity. The implications of these results are explored in the next section.

4 | Discussion

It is often expected that EPE spatial scale and intensity vary together, because large-scale environments that favour heavy

precipitation also tend to support broader rainfall coverage. For example, Zhou et al. (2013) found higher mid-level relative humidity to be associated with larger rainfall amounts and broader rainfall coverage. However, our results reveal a more complex behaviour of EPE spatial scales, both in their response to ENSO and in their long-term trends.

One possible explanation lies in the nature of the storm systems that produce extreme rainfall. Physically, the spatial scale of EPEs is strongly influenced by storm type: convective systems typically produce highly localised extremes, whereas synoptic systems like fronts can generate more widespread rainfall (e.g., Grazzini et al. 2020). Variations in the frequency of these storm types can therefore modify EPE spatial scales independently of changes in rainfall intensity. This mechanism may help explain the long-term decreasing trends observed in MAM across eastern and southeastern regions (Victoria and the East Coast; Figure 13b). Although several studies have argued that a warming climate generally favours more convective systems that concentrate rainfall over smaller areas (e.g., Peleg et al. 2018; Lochbihler et al. 2019), the fact that this

trend is most evident in MAM suggests a role for seasonally specific storm-type and large-scale circulation changes, possibly linked to the drying trend documented by CSIRO and Bureau Meteorology (2024). For example, Pepler et al. (2020) showed that the thunderstorm-only weather type contributes a relatively larger fraction of total rainfall in MAM in southern Australia. Taken together with our results in Figure 13b, this may suggest an increased influence of convective systems during this season. Further work is required to determine if such a shift in rain type is occurring in the relevant regions, especially using higher spatial resolution observations that can resolve storm morphology, such as precipitation estimates from radar or satellites.

On the other hand, the increasing length scales in SON in the same regions could be due to a seasonal shift in large-scale circulation, causing the synoptic systems that produce widespread precipitation to occur earlier in the year and/or extend further inland. Although P90 thresholds show weak trends in coastal areas, increasing values at inland stations (Figures 13d and S11) may indicate a broader inland shift in precipitation patterns. Confirming whether these contrasting shifts in EPE length scale and EPE intensity can be explained by shifts in large-scale circulation will require further investigation into the relationship between large-scale atmospheric conditions and EPE spatial characteristics.

While the semivariogram approach is useful to estimate the climatological length scales of EPEs, it assumes isotropy, meaning that the spatial correlation of precipitation decays uniformly in all directions. This isotropy assumption has two key limitations. First, the method does not account for topographic influences. For example, when a large weather system interacts with a mountain range, it can produce intense orographic precipitation on the windward side and a pronounced rain shadow on the leeward side. Our analysis would interpret this as a smaller-scale EPE, failing to distinguish it from a genuinely localised convective storm, even though their physical drivers differ fundamentally. Second, an isotropic framework cannot capture anisotropic (e.g., elongated) precipitation footprints, such as a long but narrow swath of heavy rain produced by a fast-moving, small-scale storm. This effect may be particularly noticeable in regions like the Wet Tropics, where the narrow landmass, when aligned with the prevailing flow, can enhance anisotropy. The isotropic method averages this footprint into a single length scale, losing important information about the storm's shape and motion. Accounting for anisotropy is important because the footprint's geometry reflects an EPE's physical drivers and affects its hydrological consequences, such as whether it causes localised or widespread flooding.

A further limitation is in the choice of the theoretical semivariogram model, which can influence the estimated length scales. In this study, the selection was made heuristically using synthetic data, while the optimal model for a more accurate estimation of length scales may vary across different parts of Australia. Future work should incorporate improved model selection procedures alongside methods that capture anisotropic precipitation patterns to better represent the spatial characteristics of EPEs (see, e.g., Johnston et al. 2001;

Niemi et al. 2014; Saunders et al. 2021; Verbovšek 2024, and references therein).

5 | Conclusions

We analysed the long-term climatological length scale of EPEs in Australia using the relaxed neighbourhood semivariogram approach. BoM station data from 1940 to 2024 were used to estimate the seasonal length scale of EPEs. Australia was divided into 15 regions based on the NRM clusters. The seasonal analysis reveals diverse characteristics in EPE length scales across Australia, with geographically coherent patterns emerging among adjacent regions. The seasonality differs across climate zones. Monsoon-impacted regions exhibit a visible separation between dry and wet seasons in the number of EPEs, while other regions display a clear seasonal cycle in climatological length scales. Although Tasmania is associated with the smallest length scale, it still shares geographical similarity in the seasonal cycle of length scales with nearby regions. The southern regions coincide with the smallest length scale in JJA, while the eastern regions present the largest length scale in JJA. The paired Wilcoxon signed-rank test and Mann-Whitney U test were carried out to show that the variations in the median climatological length scale are statistically significant across seasons and regions.

Based on the SOI, we present the first climatological analysis of EPE spatial scales in Australia during different ENSO phases. Although La Niña conditions are typically associated with increased precipitation in eastern Australia, our results show that EPEs are not uniformly larger in spatial scale during La Niña compared to El Niño across all seasons and all regions. In MAM, the La Niña EPEs mostly display a smaller length scale than their El Niño counterparts on the east coast, while this pattern is reversed in other seasons.

With the availability of long-term data, we also examined changes in the climatological length scale by splitting the analysis into two periods, one from 1960 to 1991 and the other from 1992 to 2023. Regardless of the Millennium drought, the analysis reveals a reduction in the spatial scale of EPEs in several regions in southeastern and eastern Australia in MAM, but an increase in SON. Crucially, these trends, along with the ENSO relationships, differ from those observed in mean precipitation and intensity of extreme precipitation in many regions, especially in DJF and JJA. This suggests that the mechanisms governing the spatial scale of extremes are distinct from those controlling mean precipitation, and that changes in mean precipitation do not necessarily imply corresponding changes in the spatial extent of extreme events.

In summary, this study provides a valuable climatological reference for the spatial extent of EPEs in Australia. By establishing how EPE spatial scales vary, we lay the foundation for future work to investigate the underlying physical mechanisms. For example, while our results suggest a link between frontal systems and large-scale EPEs in southwestern Australia in JJA, whether such systems are directly responsible for large-scale extremes in this region remains an open question. Similarly, we reveal a complex relationship between EPE spatial scales

and climate drivers like ENSO. This complexity highlights that improving projections of extreme events in a changing climate requires more than just understanding changes in mean rainfall. An important future direction is therefore to go beyond the climatological analysis here and investigate how day-to-day large-scale atmospheric conditions modulate the spatial characteristics of EPEs, and the physical mechanisms driving this modulation. Such work will strengthen the physical basis of our projections for how extreme rainfall will change in a warming climate.

Author Contributions

Dongqi Lin: conceptualization, investigation, writing – original draft, methodology, writing – review and editing, visualization, data curation, formal analysis, validation, and software. **Kate R. Saunders:** conceptualization, investigation, methodology, supervision, funding acquisition, resources, writing – review and editing. **Martin S. Singh:** conceptualization, investigation, funding acquisition, writing – review and editing, project administration, supervision, and resources.

Acknowledgements

We acknowledge the resources and support provided by the Australian National Computational Infrastructure (NCI). NCI was used for data storage and analysis presented in this study. D.L. and K.R.S. were supported by the Australian Research Council (ARC) Centre of Excellence for Climate Extremes (ARC Project CE170100023). M.S.S. received support from the ARC through the Centre of Excellence for the Weather of the 21st Century (CE230100012). Generative AI tools (ChatGPT) were used solely for language polishing and grammar refinement during the preparation of this manuscript. All AI-assisted content was carefully reviewed and edited, and the authors take full responsibility for the final version of this publication. Open access publishing facilitated by Monash University, as part of the Wiley - Monash University agreement via the Council of Australasian University Librarians

Funding

This work was supported by Australian Research Council, CE170100023, CE230100012.

Conflicts of Interest

The authors declare no conflicts of interest.

Data Availability Statement

The BoM daily rain gauge data are freely available from BoM's weather station directory (<http://www.bom.gov.au/climate/data/stations/>; last accessed: 26 August 2025). The SOI was obtained from the BoM (<http://www.bom.gov.au/climate/enso/soi/>; last accessed: 26 August 2025). The code for semivariogram estimation and the gridded maps used to create the figures in this paper are archived by Lin (2025). Figures in this paper were produced using the scientific colour maps of Crameri et al. (2020).

References

Alexander, L. V., M. Bador, R. Roca, S. Contractor, M. G. Donat, and P. L. Nguyen. 2020. "Intercomparison of Annual Precipitation Indices and Extremes Over Global Land Areas From In Situ, Space-Based and Reanalysis Products." *Environmental Research Letters* 15, no. 5: 55002.

Ashouri, H., K.-L. Hsu, S. Sorooshian, et al. 2015. "Persiann-CDR: Daily Precipitation Climate Data Record From Multisatellite Observations

for Hydrological and Climate Studies." *Bulletin of the American Meteorological Society* 96, no. 1: 69–83.

Berghuijs, W. R., S. T. Allen, S. Harrigan, and J. W. Kirchner. 2019. "Growing Spatial Scales of Synchronous River Flooding in Europe." *Geophysical Research Letters* 46, no. 3: 1423–1428.

Bevacqua, E., T. G. Shepherd, P. A. Watson, S. Sparrow, D. Wallom, and D. Mitchell. 2021. "Larger Spatial Footprint of Wintertime Total Precipitation Extremes in a Warmer Climate." *Geophysical Research Letters* 48, no. 8: e2020GL091990.

Bevacqua, E., G. Zappa, and T. G. Shepherd. 2020. "Shorter Cyclone Clusters Modulate Changes in European Wintertime Precipitation Extremes." *Environmental Research Letters* 15, no. 12: 124005.

Bowden, A., C. Jakob, and J. Soderholm. 2025. "Stormy Subtropics and Stratiform South: Radar-Based Classification and Analysis of Australian Rainfall Events." *Journal of Geophysical Research: Atmospheres* 130, no. 2: e2024JD041790.

Chang, W., M. L. Stein, J. Wang, V. R. Kotamarthi, and E. J. Moyer. 2016. "Changes in Spatiotemporal Precipitation Patterns in Changing Climate Conditions." *Journal of Climate* 29, no. 23: 8355–8376.

Chung, C. T., and S. B. Power. 2017. "The Non-Linear Impact of el niño, la niña and the Southern Oscillation on Seasonal and Regional Australian Precipitation." *Journal of Southern Hemisphere Earth Systems Science* 67, no. 1: 25–45.

Crameri, F., G. E. Shephard, and P. J. Heron. 2020. "The Misuse of Colour in Science Communication." *Nature Communications* 11, no. 1: 5444.

Cressie, N. 2015. *Statistics for Spatial Data*. John Wiley & Sons.

CSIRO. 2015. *Climate Change in Australia, Technical Report: Projections for Australia's Nrm Regions*. Commonwealth Scientific and Industrial Research Organisation and Australian Bureau of Meteorology Marine and Atmospheric Research Melbourne.

CSIRO, & Bureau of Meteorology. 2024. "State of the Climate 2024."

Dey, R., S. C. Lewis, J. M. Arblaster, and N. J. Abram. 2019. "A Review of Past and Projected Changes in Australia's Rainfall." *Wiley Interdisciplinary Reviews: Climate Change* 10, no. 3: e577.

Domeisen, D. I., C. J. White, H. Afargan-Gerstman, et al. 2022. "Advances in the Subseasonal Prediction of Extreme Events: Relevant Case Studies Across the Globe." *Bulletin of the American Meteorological Society* 103, no. 6: E1473–E1501.

Drosowsky, W. 1993. "An Analysis of Australian Seasonal Rainfall Anomalies: 1950–1987. I: Spatial Patterns." *International Journal of Climatology* 13, no. 1: 1–30.

Dunn, R. E., H. J. Fowler, A. C. Green, and E. Lewis. 2025. "Tipping-Bucket Rain Gauges: A Review of the Undercatch Phenomenon, and Methods for Its Reduction and Correction." *Weather* 80: 196–205.

Dwyer, J., and P. O'Gorman. 2017. "Changing Duration and Spatial Extent of Midlatitude Precipitation Extremes Across Different Climates." *Geophysical Research Letters* 44, no. 11: 5863–5871.

Evans, A., D. Jones, R. Smalley, and S. Lellyett. 2020. "An Enhanced Gridded Rainfall Analysis Scheme for Australia." *Australian Bureau of Meteorology* 66: 55–67.

Gillett, Z., A. Taschetto, C. Holgate, and A. Santoso. 2023. "Linking Enso to Synoptic Weather Systems in Eastern Australia." *Geophysical Research Letters* 50, no. 15: e2023GL104814.

Grazzini, F., G. C. Craig, C. Keil, G. Antolini, and V. Pavan. 2020. "Extreme Precipitation Events Over Northern Italy. Part I: A Systematic Classification With Machine-Learning Techniques." *Quarterly Journal of the Royal Meteorological Society* 146, no. 726: 69–85.

Guinard, K., A. Maillhot, and D. Caya. 2015. "Projected Changes in Characteristics of Precipitation Spatial Structures Over North America." *International Journal of Climatology* 35, no. 4: 596–612

- He, J., S. Li, B. Wang, L. Zhang, and K. Duan. 2025. "Quantifying the Impacts of Enso on Australian Summer Rainfall Extremes During 1960–2020." *Journal of Hydrology* 654: 1–17.
- Hoegh-Guldberg, O., D. Jacob, M. Taylor, et al. 2018. "Impacts of 1.5°C Global Warming on Natural and Human Systems." In *An IPCC Special Report on the Impacts of Global Warming of 1.5°C Above Pre-Industrial Levels and Related Global Greenhouse Gas Emission Pathways, in the Context of Strengthening the Global Response to the Threat of Climate Change, Sustainable Development, and Efforts to Eradicate Poverty*, 175–311. Intergovernmental Panel on Climate Change (IPCC).
- Huang, A. T., Z. E. Gillett, and A. S. Taschetto. 2024. "Australian Rainfall Increases During Multi-Year la niña." *Geophysical Research Letters* 51, no. 9: e2023GL106939.
- Irving, D. B., J. S. Risbey, D. T. Squire, et al. 2024. "A Multi-Model Likelihood Analysis of Unprecedented Extreme Rainfall Along the East Coast of Australia." *Meteorological Applications* 31, no. 3: e2217.
- Jackson, R. C., S. M. Collis, V. Louf, A. Protat, and L. Majewski. 2018. "A 17 Year Climatology of the Macrophysical Properties of Convection in Darwin." *Atmospheric Chemistry and Physics* 18, no. 23: 17687–17704.
- Johnston, K., J. M. Ver Hoef, K. Krivoruchko, and N. Lucas. 2001. *Using Arcgis Geostatistical Analyst*. Vol. 380. Environmental Systems Research Institute Inc.
- Jones, D. A., W. Wang, and R. Fawcett. 2009. "High-Quality Spatial Climate Datasets for Australia." *Australian Meteorological and Oceanographic Journal* 58, no. 4: 233.
- Jongman, B., S. Hochrainer-Stigler, L. Feyen, et al. 2014. "Increasing Stress on Disaster-Risk Finance due to Large Floods." *Nature Climate Change* 4, no. 4: 264–268.
- Khouakhi, A., G. Villarini, and G. A. Vecchi. 2017. "Contribution of Tropical Cyclones to Rainfall at the Global Scale." *Journal of Climate* 30, no. 1: 359–372.
- King, A. D., L. V. Alexander, and M. G. Donat. 2013. "The Efficacy of Using Gridded Data to Examine Extreme Rainfall Characteristics: A Case Study for Australia." *International Journal of Climatology* 33, no. 10: 2376–2387.
- King, A. D., N. P. Klingaman, L. V. Alexander, M. G. Donat, N. C. Jourdain, and P. Maher. 2014. "Extreme Rainfall Variability in Australia: Patterns, Drivers, and Predictability." *Journal of Climate* 27, no. 15: 6035–6050.
- King, A. D., A. J. Pitman, B. J. Henley, A. M. Ukkola, and J. R. Brown. 2020. "The Role of Climate Variability in Australian Drought." *Nature Climate Change* 10, no. 3: 177–179.
- Lin, D. 2025. *Semi-Variogram AU: Semivariogram v1.1 With Gridded Map*. Zenodo. <https://doi.org/10.5281/zenodo.16946013>.
- Lochbihler, K., G. Lenderink, and A. P. Siebesma. 2017. "The Spatial Extent of Rainfall Events and Its Relation to Precipitation Scaling." *Geophysical Research Letters* 44, no. 16: 8629–8636.
- Lochbihler, K., G. Lenderink, and A. P. Siebesma. 2019. "Response of Extreme Precipitating Cell Structures to Atmospheric Warming." *Journal of Geophysical Research: Atmospheres* 124, no. 13: 6904–6918.
- Mann, H. B., and D. R. Whitney. 1947. "On a Test of Whether One of Two Random Variables Is Stochastically Larger Than the Other." *Annals of Mathematical Statistics* 18: 50–60.
- McBride, J. L., and N. Nicholls. 1983. "Seasonal Relationships Between Australian Rainfall and the Southern Oscillation." *Monthly Weather Review* 111, no. 10: 1998–2004.
- McGregor, S., A. Gallant, and P. van Rensch. 2024. "Quantifying Ensos Impact on Australia's Regional Monthly Rainfall Risk." *Geophysical Research Letters* 51, no. 6: e2023GL106298.
- Montoya Duque, E., Y. Huang, P. May, and S. Siems. 2023. "An Evaluation of Imerg and era5 Quantitative Precipitation Estimates Over the Southern Ocean Using Shipborne Observations." *Journal of Applied Meteorology and Climatology* 62, no. 11: 1479–1495.
- Müller, S., L. Schüler, A. Zech, and F. Heße. 2022. "GSTools v1.3: A Toolbox for Geostatistical Modelling in Python." *Geoscientific Model Development* 15, no. 7: 3161–3182. <https://doi.org/10.5194/gmd-15-3161-2022>.
- Nicholls, N., W. Drosowsky, and B. Lavery. 1997. "Australian Rainfall Variability and Change." *Weather* 52, no. 3: 66–72.
- Niemi, T. J., T. Kokkonen, and A. W. Seed. 2014. "A Simple and Effective Method for Quantifying Spatial Anisotropy of Time Series of Precipitation Fields." *Water Resources Research* 50, no. 7: 5906–5925.
- Nikumbh, A. C., A. Chakraborty, and G. Bhat. 2019. "Recent Spatial Aggregation Tendency of Rainfall Extremes Over India." *Scientific Reports* 9, no. 1: 10321.
- O'Gorman, P. A. 2015. "Precipitation Extremes Under Climate Change." *Current Climate Change Reports* 1: 49–59.
- O'Gorman, P. A., and T. Schneider. 2009. "The Physical Basis for Increases in Precipitation Extremes in Simulations of 21st-Century Climate Change." *Proceedings of the National Academy of Sciences* 106, no. 35: 14773–14777.
- Paciorek, C. J., D. A. Stone, and M. F. Wehner. 2018. "Quantifying Statistical Uncertainty in the Attribution of Human Influence on Severe Weather." *Weather and Climate Extremes* 20: 69–80.
- Peleg, N., F. Marra, S. Fatichi, et al. 2018. "Intensification of Convective Rain Cells at Warmer Temperatures Observed From High-Resolution Weather Radar Data." *Journal of Hydrometeorology* 19, no. 4: 715–726.
- Pepler, A. S., A. J. Dowdy, P. Van Rensch, I. Rudeva, J. L. Catto, and P. Hope. 2020. "The Contributions of Fronts, Lows and Thunderstorms to Southern Australian Rainfall." *Climate Dynamics* 55: 1489–1505.
- Ponukumati, P., A. Mohammed, and S. Regonda. 2023. "Insights on Satellite-Based Imerg Precipitation Estimates at Multiple Space and Time Scales for a Developing Urban Region in India." *Journal of Hydrometeorology* 24, no. 6: 977–996.
- Pook, M. J., J. S. Risbey, and P. C. McIntosh. 2012. "The Synoptic Climatology of Cool-Season Rainfall in the Central Wheatbelt of Western Australia." *Monthly Weather Review* 140, no. 1: 28–43.
- Pope, M., C. Jakob, and M. J. Reeder. 2008. "Convective Systems of the North Australian Monsoon." *Journal of Climate* 21, no. 19: 5091–5112.
- Prescott, J. A., J. A. Collins, and G. Shirpurkar. 1952. "The Comparative Climatology of Australia and Argentina." *Geographical Review* 42, no. 1: 118–133. <https://doi.org/10.2307/211256>.
- Raut, B. A., C. Jakob, and M. J. Reeder. 2014. "Rainfall Changes Over Southwestern Australia and Their Relationship to the Southern Annular Mode and Enso." *Journal of Climate* 27, no. 15: 5801–5814.
- Risbey, J. S., M. J. Pook, P. C. McIntosh, M. C. Wheeler, and H. H. Hendon. 2009. "On the Remote Drivers of Rainfall Variability in Australia." *Monthly Weather Review* 137, no. 10: 3233–3253.
- Saunders, K., A. Stephenson, and D. Karoly. 2021. "A Regionalisation Approach for Rainfall Based on Extremal Dependence." *Extremes* 24: 215–240.
- Schaller, N., A. L. Kay, R. Lamb, et al. 2016. "Human Influence on Climate in the 2014 Southern England Winter Floods and Their Impacts." *Nature Climate Change* 6, no. 6: 627–634.
- Schumacher, R. S. 2017. "Heavy Rainfall and Flash Flooding." In *Oxford Research Encyclopedia of Natural Hazard Science*. Oxford University Press.
- Simpson, J., C. Kummerow, W. K. Tao, and R. F. Adler. 1996. "On the Tropical Rainfall Measuring Mission (TRMM)." *Meteorology and Atmospheric Physics* 60: 19–36.
- Tan, X., X. Wu, and B. Liu. 2021. "Global Changes in the Spatial Extents of Precipitation Extremes." *Environmental Research Letters* 16, no. 5: 54017.

- Tansey, E., R. Marchand, A. Protat, S. P. Alexander, and S. Ding. 2022. "Southern Ocean Precipitation Characteristics Observed From Cloudsat and Ground Instrumentation During the Macquarie Island Cloud & Radiation Experiment (Micre): April 2016 to March 2017." *Journal of Geophysical Research: Atmospheres* 127, no. 5: e2021JD035370.
- Touma, D., A. M. Michalak, D. L. Swain, and N. S. Diffenbaugh. 2018. "Characterizing the Spatial Scales of Extreme Daily Precipitation in the United States." *Journal of Climate* 31, no. 19: 8023–8037.
- Touma, D., S. Stevenson, S. J. Camargo, D. E. Horton, and N. S. Diffenbaugh. 2019. "Variations in the Intensity and Spatial Extent of Tropical Cyclone Precipitation." *Geophysical Research Letters* 46, no. 23: 13992–14002.
- Tozer, C. R., J. S. Risbey, D. P. Monselesan, et al. 2023. "Impacts of Enso on Australian Rainfall: What Not to Expect." *Journal of Southern Hemisphere Earth Systems Science* 73, no. 1: 77–81.
- Tozer, C. R., J. S. Risbey, T. J. O'Kane, D. P. Monselesan, and M. J. Pook. 2018. "The Relationship Between Wave Trains in the Southern Hemisphere Storm Track and Rainfall Extremes Over Tasmania." *Monthly Weather Review* 146, no. 12: 4201–4230.
- Trenberth, K. E. 1984. "Signal Versus Noise in the Southern Oscillation." *Monthly Weather Review* 112, no. 2: 326–332.
- Van Dijk, A. I., H. E. Beck, R. S. Crosbie, et al. 2013. "The Millennium Drought in Southeast Australia (2001–2009): Natural and Human Causes and Implications for Water Resources, Ecosystems, Economy, and Society." *Water Resources Research* 49, no. 2: 1040–1057.
- Verbovšek, T. 2024. "Analysis of Karst Surface Anisotropy Using Directional Semivariograms, Slovenia." *Pure and Applied Geophysics* 181, no. 1: 233–245.
- Virtanen, P., R. Gommers, T. E. Oliphant, et al. 2020. "SciPy 1.0: Fundamental Algorithms for Scientific Computing in Python." *Nature Methods* 17: 261–272. <https://doi.org/10.1038/s41592-019-0686-2>.
- Warren, R. A., C. Jakob, S. M. Hitchcock, and B. A. White. 2021. "Heavy Versus Extreme Rainfall Events in Southeast Australia." *Quarterly Journal of the Royal Meteorological Society* 147, no. 739: 3201–3226.
- Wasko, C., A. Sharma, and S. Westra. 2016. "Reduced Spatial Extent of Extreme Storms at Higher Temperatures." *Geophysical Research Letters* 43, no. 8: 4026–4032.
- Webster, R., and M. A. Oliver. 2007. *Geostatistics for Environmental Scientists*. John Wiley & Sons.
- White, B., C. Jakob, and M. Reeder. 2022. "Fundamental Ingredients of Australian Rainfall Extremes." *Journal of Geophysical Research: Atmospheres* 127, no. 17: e2021JD036076.
- Wilcoxon, F. 1945. "Individual Comparisons by Ranking Methods." *Biometrics Bulletin* 1, no. 6: 80–83. <https://doi.org/10.2307/3001968>.
- Zhou, Y., W. K. Lau, and C. Liu. 2013. "Rain Characteristics and Large-Scale Environments of Precipitation Objects With Extreme Rain Volumes From Trmm Observations." *Journal of Geophysical Research: Atmospheres* 118, no. 17: 9673–9689.

Supporting Information

Additional supporting information can be found online in the Supporting Information section. **Data S1:** Supporting Information.